Two opposite voltage-dependent currents control the unusual early development pattern of embryonic Renshaw cell electrical activity

Juliette Boeri[1¶], Claude Meunier[2 ¶], Hervé Le Corronc[1,3 ¶], Pascal Branchereau[4], Yulia Timofeeva[2,5,6], François Xavier Lejeune[7], Christine Mouffle[1], Hervé Arulkandarajah[1], Jean Marie Mangin[1], Pascal Legendre[1&]*, Antonny Czarnecki[1,4&]*

Affiliation

[1] INSERM, UMR_S 1130, CNRS, UMR 8246, Neuroscience Paris Seine, Institute of Biology Paris Seine, Sorbonne Univ, Paris, France.
[2] Centre de Neurosciences Intégratives et Cognition, CNRS UMR 8002, Institut Neurosciences et Cognition, Université de Paris, Paris, France.
[3] Univ Angers, Angers, France.
[4] Univ. Bordeaux, CNRS, EPHE, INCIA, UMR 5287 F-33000 Bordeaux, France
[5] Department of Computer Science and Centre for Complexity Science, University of Warwick, Coventry, UK.
[6] Department of Clinical and Experimental Epilepsy, UCL Queen Square Institute of Neurology, University College London, London, UK.
[7] Institut du Cerveau et de la Moelle Epinière, Centre de Recherche CHU Pitié-Salpétrière, INSERM, U975, CNRS, UMR 7225, Sorbonne Univ, Paris, France.

* Corresponding authors
Email: pascal.legendre@inserm.fr (PL)
Email: antonny.czarnecki@u-bordeaux.fr (AC)

[¶]These authors contributed equally to this work.

[&]These authors also contributed equally to this work.

Abstract

Renshaw cells (V1R) are excitable as soon as they reach their final location next to the spinal motoneurons and display heterogeneous activity patterns at the onset of the synaptogenesis (12 days post-fertilization; E12.5). Using multiple experimental approaches, in combination with biophysical modeling and dynamical systems theory, we analyzed, for the first time, the mechanisms underlying the electrophysiological properties of V1R during early embryonic development of the spinal cord locomotor networks (E11.5-E16.5). We found that these interneurons are subdivided into several functional clusters from E11.5 and then display an unexpected transitory involution process during which they lose their ability to sustain tonic firing. V1R begin to recover this capability when a locomotor-like activity emerges (after E15.5). Our computational analysis, closely based on experimental data, demonstrated that the essential factor controlling the diversity of the discharge pattern of embryonic V1R is the ratio of a persistent sodium conductance to a delayed rectifier potassium conductance. We also found that V1R involution is due to a decrease of the persistent sodium conductance as V1R develop and their size increases. Taken together, our results reveal how a simple mechanism, based on the synergy of two voltage-dependent conductances that are ubiquitous in neurons, can produce functional diversity in V1R and control their early developmental trajectory. Our findings also indicate that homeostatic regulation of channel density or channel degeneracy known to maintain homogeneous firing pattern within specific populations of mature neurons, are unlikely to occur at these early developmental stages.

Keywords: development, spinal cord, embryo, Renshaw cell, firing pattern, functional involution, electrophysiology, biophysical modeling.

56 ## Introduction

57 The development of the central nervous system (CNS) follows complex steps, which depend
58 on genetic and environmental factors and involve interactions between multiple elements of
59 the neural tissue. Remarkably, emergent neurons begin to synchronize soon after the onset
60 of synapse formation, generating long episodes of low frequency (<0.01 Hz) correlated
61 spontaneous network activity (SNA) [1-8]. In the mouse embryonic spinal cord (SC), SNA is
62 driven by an excitatory cholinergic-GABAergic loop between motoneurons (MNs) and
63 interneurons (INs), GABA being depolarizing before embryonic day 16.5 (E16.5) [9]. SNA
64 emerges around E12.5 [4, 6, 10-12], at a time when functional neuromuscular junctions are
65 not yet established [13], and sensory and supraspinal inputs have not yet reached the spinal
66 motor networks [14-17].

67 Several studies pointed out that SNA is an essential component in neuronal networks
68 formation. [18-21]. In the SC, pharmacologically-induced disturbances of SNA between E12.5
69 and E14.5 induce defects in the formation of motor pools, in motor axon guidance to their
70 target muscles and in the development of motor networks [4, 21-23]. During SNA episodes,
71 long lasting giant depolarization potentials (GDPs) are evoked in the SC, mainly by the
72 massive release of GABA onto MNs [12]. Immature Renshaw cells ($V1^R$) are likely the first
73 GABAergic partners of MNs in the mouse embryo [24, 25], and the massive release of GABA
74 during SNA probably requires that many of them display repetitive action potential firing or
75 plateau potential activity [25].

76 However, little is known about the firing pattern of embryonic $V1^R$ and the maturation of
77 their intrinsic properties. We recently found that $V1^R$ exhibit heterogeneous excitability
78 properties when SNA emerges in the SC [25] in contrast to adult Renshaw cells that
79 constitute a functionally homogeneous population [26, 27]. Whether this early functional

80 diversity really reflects distinct functional classes of $V1^R$, how this diversity evolves during
81 development, and what are the underlying biophysical mechanisms remain open questions.
82 The present study addresses these issues using multiple approaches, including patch-clamp
83 recordings, cluster analysis, biophysical modeling and dynamical systems theory. The firing
84 patterns of $V1^R$ and the mechanisms underlying their functional diversity are analyzed during
85 a developmental period covering the initial phase of development of SC activity in the
86 mouse embryo (E11.5-E14.5), when SNA is present, and during the critical period (E14.5-
87 E16.5), when GABAergic neurotransmission gradually shifts from excitation to inhibition [28]
88 and locomotor-like activity emerges [4, 10, 11].
89 We discover that the balance between the slowly inactivating subthreshold persistent
90 sodium inward current (I_{Nap}) [29] and the delayed rectifier potassium outward current
91 (I_{Kdr}), accounts for the heterogeneity of embryonic $V1^R$ and the changes in firing pattern
92 during development. The heterogeneity of $V1^R$ at E12.5 arises from the existence of distinct
93 functional groups. Surprisingly, and in opposition to the classically accepted development
94 scheme [30-35], we show that the embryonic $V1^R$ population loses its ability to support tonic
95 firing from E13.5 to E15.5, exhibiting a transient functional involution during its
96 development. Our experimental and theoretical results provide a global view of the
97 developmental trajectories of embryonic $V1^R$. They demonstrate that a simple mechanism,
98 based on the synergy of only two major opposing voltage-dependent currents, accounts for
99 functional diversity in these immature neurons.
100

101 # Results

102 **The delayed rectifier potassium current I_{Kdr} is a key partner of the persistent sodium**
103 **current I_{Nap} in controlling embryonic $V1^R$ firing patterns during development**

104 We previously highlighted that V1^R are spontaneously active at E12.5. Their response to a 2 s
105 suprathreshold depolarizing current steps revealed four main patterns, depending of the
106 recorded interneuron [25]: i) single spiking (SS) V1^R that fires only 1-3 APs at the onset of the
107 depolarizing pulse, ii) repetitive spiking (RS) V1^R, iii) mixed events (ME) V1^R that shows an
108 alternation of action potentials (APs) and plateau potentials or, iv) V1^R that displays a long-
109 lasting sodium-dependent plateau potential (PP) (***Figure 1A1–A4***).
110 We also uncovered a relationship between I_{Nap} and the ability of embryonic V1^R to sustain
111 repetitive firing [25]. However, the heterogeneous firing patterns of V1^R observed at E12.5
112 could not be fully explained by variations in I_{Nap} [25], suggesting the involvement of other
113 voltage-gated channels in the control of the firing pattern of V1^R, in particular potassium
114 channels, known to control firing and AP repolarization. Our voltage clamp protocol,
115 performed in the presence of TTX (1 μM), did not disclose any inward rectifying current
116 (hyperpolarizing voltage steps to -100 mV from V_H = -20 mV, data not shown), but revealed
117 two voltage-dependent outward potassium currents, a delayed rectifier current (I_{Kdr}) and a
118 transient potassium current (I_A) in all embryonic V1^R, whatever the firing pattern (***Figure***
119 ***1B1–B4***). These currents are known to control AP duration (I_{Kdr}) or firing rate (I_A),
120 respectively [36]. The activation threshold of I_{Kdr} lied between -30 mV and -20 mV and the
121 threshold of I_A between -60 mV and -50 mV, (n = 27; N = 27 embryos) (***Figure 1C1–C4***).
122 Removing external calcium had no effect on potassium current I/V curves (data not shown),
123 suggesting that calcium-dependent potassium currents are not yet present at E12.5.
124 It was unlikely that the heterogeneity of V1^R firing patterns resulted from variations in the
125 intensity of I_A. Indeed, its voltage-dependent inactivation (time constant: 23.3 ± 2.6 ms, n =
126 8; N = 8), which occurs during the depolarizing phase of an AP, makes it ineffective to control
127 AP or plateau potential durations. This was confirmed by our theoretical analysis (***see Figure***

128 ***7—figure supplement 1***). We thus focused our study on I_{Kdr}. At E12.5, PP V1^R had a
129 significantly lower G_{Kdr} (2.12 ± 0.44 nS, n = 6; N = 6) than SS V1^R (5.57 ± 0.56 nS, n = 9; N = 9)
130 and RS V1^R (6.39 ± 0.83 nS, n = 7; N = 7) (***Figure 1D***). However, there was no significant
131 difference in G_{Kdr} between SS V1^R and RS V1^R at E12.5 (***Figure 1D***), which indicated that
132 variations in G_{Kdr} alone could not explain all the firing patterns observed at E12.5. Similarly,
133 there was no significant difference in G_{Nap} between RS V1^R (0.91 ± 0.21nS, n = 8; N = 8) and
134 PP V1^R (1.24 ± 0.19 nS, n = 6; N = 6) at E12.5 (***Figure 1E***), indicating that variations
135 in G_{Nap} alone could not explain all the firing patterns of V1^R at E12.5 [25]. In contrast
136 G_{Nap} measured in SS V1^R at E12.5 (0.21 ± 0.20 nS, n = 9; N = 9) were significantly lower
137 compared to G_{Nap} measured in RS V1^R and in PP V1^R at E12.5 (***Figure 1E***).
138 Mature neurons often display multiple stable firing patterns [37-39]. This usually depends on
139 the combination of several outward and inward voltage- or calcium-dependent
140 conductances and on their spatial localization [37-39]. In contrast, immature V1^R have a
141 limited repertoire of voltage-dependent currents (I_{Nat} and I_{Nap}, I_{Kdr} and I_A) at E12.5, and
142 we did not find any evidence of voltage-dependent calcium currents at this age [25].
143 Blocking I_{Nap} prevented plateau potential activity, PP-V1^R becoming unexcitable, and turned
144 repetitive spiking V1^R into single spiking V1^R [25]. Therefore, we hypothesized that the
145 different firing patterns of V1^R observed at E12.5 were related to the G_{Nap} / G_{Kdr} ratio only,
146 with variations in the intensity of I_A being unlikely to account for the heterogeneity of firing
147 pattern. We found that this ratio was significantly lower for SS V1^R recorded at E12.5
148 (G_{Nap} / G_{Kdr} = 0.043 ± 0.015, n = 9) compared to RS V1^R (0.154 ± 0.022, n = 8) and PP V1^R
149 (0.66 ± 0.132, n = 6) (***Figure 1F***). We also found that the G_{Nap} / G_{Kdr} ratio was significantly
150 lower for RS V1^R compared to PP V1^R (***Figure 1F***).

151 Altogether, these results strongly suggest that, although the presence of I_{Nap} is required for
152 embryonic V1^R to fire repetitively or to generate plateau potentials [25], the heterogeneity
153 of the firing pattern observed between E12.5 is not determined by I_{Nap} *per se* but likely by
154 the balance between I_{Nap} and I_{Kdr}.
155
156 **Manipulating the balance between G_{Nap} and G_{Kdr} changes embryonic V1^R firing patterns**
157 We previously showed that blocking I_{Nap} with riluzole converted PP V1^R or RS V1^R into SS
158 V1^R [25]. To confirm further that the balance between G_{Nap} and G_{Kdr} was the key factor in
159 the heterogeneity of V1^R firing patterns, we assessed to what extent a given E12.5 SS V1^R cell
160 could change its firing pattern when I_{Kdr} was gradually blocked by 4-aminopiridine (4-AP).
161 We found that I_{Kdr} could be blocked by micromolar concentrations of 4-AP without
162 affecting I_A (***Figure 2—figure supplement 1***). 4-AP, applied at concentrations ranging from
163 0.3 μM to 300 μM, specifically inhibited I_{Kdr} with an IC_{50} of 2.9 μM (***Figure 2—figure***
164 ***supplement 1C1***).
165 We then determined to what extent increasing the concentration of 4-AP modified the firing
166 pattern of V1^R at E12.5. Applying 4-AP at concentrations ranging from 3 μM to 300 μM
167 changed the firing pattern of SS V1^R (n = 10; N = 10) in a concentration-dependent manner
168 (***Figure 2A1–A3***). In 50% of the recorded V1^R, increasing 4-AP concentrations successfully
169 transformed SS V1^R into PP V1^R with the following sequence: SS → RS → ME → PP (***Figure***
170 ***2A1***). In a second group of embryonic V1^R (25%), 4-AP application only evoked mixed activity,
171 with the same sequence as aforementioned (SS → RS → ME) (data not shown). In the
172 remaining SS V1^R (25%), increasing 4-AP concentration only led to sustained AP firing (***Figure***
173 ***2A2***). Application of 300 μM 4-AP on RS V1^R at E12.5 evoked mixed events or plateau
174 potentials (***Figure 2—figure supplement 2***). Plateau potentials and repetitive spiking evoked

175 in the presence of 300 μM 4-AP were fully blocked by 0.5-1 μM TTX, indicating that they
176 were generated by voltage-gated Na^+ channels (***Figure 2B,C*** and ***Figure 2—figure***
177 ***supplement 2***). It should be noted that the application of 300 μM of 4-AP induced a
178 significant 30.5 ± 12.4 % increase (*P* = 0.0137; Wilcoxon test) of the input resistance (1.11 ±
179 0.08 GΩ versus 1.41 ± 0.12 GΩ; n = 11; N = 11).
180 These results show that, in addition to I_{Nap}, I_{Kdr} is also a major determinant of the firing
181 pattern of embryonic $V1^R$. The above suggests that the firing patterns depend on a synergy
182 between I_{Nap} and I_{Kdr} and that the different patterns can be ordered along the following
183 sequence SS → RS → ME → PP when the ratio $G_{Nap}/\ G_{Kdr}$ is increased.
184
185 **The heterogeneity of the $V1^R$ firing patterns decreases during embryonic development**
186 It was initially unclear whether these different firing patterns corresponded to well
187 separated classes within the E12.5 $V1^R$ population or not. To address this question, we
188 performed a hierarchical cluster analysis on 163 embryonic $V1^R$, based on three quantitative
189 parameters describing the firing pattern elicited by the depolarizing pulse: the mean
190 duration of evoked APs or plateau potentials measured at half-amplitude (mean ½Ad), the
191 variability of the event duration during repetitive firing (coefficient of variation of ½Ad: CV
192 ½Ad) and the total duration of all events, expressed in percentage of the pulse duration
193 (depolarizing duration ratio: ddr) (***Figure 3A inserts***). In view of the large dispersion of mean
194 ½Ad and ddr values, cluster analysis was performed using the (decimal) logarithm of these
195 two quantities [40]. The analysis of the distribution of log mean ½Ad, CV ½Ad and log ddr
196 revealed multimodal histograms that could be fitted with several Gaussians (***Figure 3—***
197 ***figure supplement 1A1–C1***). Cluster analysis based on these three parameters showed that
198 the most likely number of clusters was 5 (***Figure 3A,B***), as determined by the silhouette

199 width measurement (***Figure 3B***). Two clearly separated embryonic $V1^R$ groups with CV ½Ad =
200 0 stood out, as shown in the 3D plot in ***Figure 5C***. The cluster with the largest ½Ad (mean
201 ½Ad = 833.5 ± 89.99 ms) and the largest ddr (0.441 ± 0.044) contained all PP $V1^R$ (n = 35; N =
202 29) (***Figure 3C-D*** and ***Figure 3—figure supplement 1A2,C2***). Similarly, the cluster with the
203 shortest ½Ad (9.73 ± 0.66 ms) and the lowest ddr (0.0051 ± 0.0004) contained all SS $V1^R$ (n =
204 46; N = 37) (***Figure 3C-D*** and ***Figure 3—figure supplement 1A2,C2***).
205 The three other clusters corresponded to $V1^R$ with nonzero values of CV ½Ad (***Figure 3C***). A
206 first cluster regrouping all RS $V1^R$ (n = 69; N = 61) was characterized by smaller values of ½Ad
207 (23.91 ± 1.43 ms), CV ½Ad (27.36 ± 1.64%) and ddr (0.11 ± 0.01) (***Figure 3C-D*** and ***Figure 3—***
208 ***figure supplement 1A2,C2***). The last two clusters corresponded to ME $V1^R$ (***Figure 3C,D***). The
209 smaller cluster, characterized by a larger CV ½Ad (170.9 ± 8.9%; n= 4; N = 4), displayed a mix
210 of APs and short plateau potentials, while the second cluster, with smaller CV ½Ad (87.61 ±
211 7.37%; n = 9; N = 9), displayed a mix of APs and long-lasting plateau potentials (***Figure 3D***
212 and ***Figure 3—figure supplement 1B2***). Their ½Ad and ddr values were not significantly
213 different (***Figure 3—figure supplement 1A2,C2***).
214 It must be noted that three embryonic $V1^R$ (1.8%) were apparently misclassified since they
215 were aggregated within the RS cluster although having zero CV ½Ad (***Figure 3C; arrows***).
216 Examination of their firing pattern revealed that this was because they generated only two
217 APs, although their ddr (0.16 to 0.2) and ½ Ad values (31.6 to 40.3 ms) were well in the range
218 corresponding of the RS cluster.
219 These different firing patterns of $V1^R$ might reflect different states of neuronal development
220 [31, 41-43]. Single spiking and/or plateau potentials are generally believed to be the most
221 immature forms of firing pattern, repetitive spiking constituting the most mature form [19,
222 44]. If it were so, the firing patterns of embryonic $V1^R$ would evolve during embryonic

223 development from single spiking or plateau potential to repetitive spiking, this latter firing
224 pattern becoming the only one in neonates [26] and at early postnatal stages [27]. However,
225 RS neurons already represent 41% of $V1^R$ at E12.5. We therefore analyzed the development
226 of firing patterns from E11.5, when $V1^R$ terminate their migration and reach their final
227 position [45], to E16.5. This developmental period covers a first phase of development
228 (E11.5-E14.5), where lumbar spinal networks exhibit SNA, and a second phase (E14.5-E16.5),
229 where locomotor-like activity emerges [4, 11, 46, 47]. We first analyzed changes in the
230 intrinsic properties (input capacitance C_{in}, input resistance $R_{in} = 1/G_{in}$ and spike voltage
231 threshold) of $V1^R$. C_{in} did not change significantly from E11.5 to E13.5 (***Figure 4A1***),
232 remaining of the order of 12 pF, in agreement with our previous work [25]. However, it
233 increased significantly at the transition between the two developmental periods (E13.5-
234 E15.5) to reach about 23.5 pF at E15.5 (***Figure 4A1***). A similar developmental pattern was
235 observed for R_{in}, which remained stable during the first phase from E11.5 to E14.5 ($R_{in} \approx$ 1-
236 1.2 GΩ) but decreased significantly after E14.5 to reach about 0.7 GΩ at E15.5 (***Figure 4A2***).
237 Spike threshold also decreased significantly between the first and the second developmental
238 phases, dropping from about -34 mV at E12.5 to about -41 mV at E16.5 (***Figure 4A3***).
239 Interestingly, this developmental transition around E14.5 correspond to the critical stage at
240 which SNA gives way to a locomotor-like activity [11, 46, 47] and rhythmic activity becomes
241 dominated by glutamate release rather than acetylcholine release [4].
242 This led us to hypothesize that this developmental transition could be also critical for the
243 maturation of $V1^R$ firing patterns. The distinct firing patterns observed at E12.5 were already
244 present at E11.5 (***Figure 4B1,C***), but the percentage of RS $V1^R$ strongly increased from E11.5
245 to E12.5, while the percentage of ME $V1^R$ decreased significantly (***Figure 4C***). The
246 heterogeneity of $V1^R$ firing patterns then substantially diminished. Plateau potentials were

247 no longer observed at E13.5 (***Figure 4B2,C***), and ME V1^R disappeared at E14.5 (***Figure 4B3,C***).
248 Interestingly, the proportion of SS V1^R remained high from E13.5 to E15.5 and even slightly
249 increased (91.23% at E14.5 and 93.33% at E15.5; ***Figure 4C***). This trend was partially
250 reversed at E16.5, as the percentage of RS V1^R increased at the expense of SS V1^R (67.86% SS
251 V1^R and 32.34% RS V1^R; ***Figure 4B5,C***). This decrease in repetitive firing capability after E13.5
252 was surprising in view of what is classically admitted on the developmental pattern of
253 neuronal excitability [18, 48]. Therefore, we verified that it did not reflect the death of some
254 V1^R after E13.5. Our data did not reveal any activated caspase3 (aCaspase3) staining in V1^R
255 (FoxD3 staining) at E14.5 (n = 10 SCs; N = 10) (***Figure 5***), in agreement with previous reports
256 showing that developmental cell death of V1^R does not occur before birth [49].
257 To determine whether G_{Nap} and G_{Kdr} also controlled the firing pattern of V1^R at E14.5 (see
258 ***Figure 4B3,C***), we assessed the presence of I_{Nap} and I_{Kdr} in single spiking V1^R at this
259 embryonic age. Both I_{Nap} and I_{Kdr} were present in V1^R at E14.5 (***Figure 6—figure***
260 ***supplement 1*** **and** ***Figure 6—figure supplement 2*****)** whereas, as in V1^R at E12.5, no calcium-
261 dependent potassium current was detected at this developmental age (not shown). In SS V1^R,
262 G_{Kdr} was significantly higher at E14.5 (11.11 ± 1.12 nS, n = 10; N = 10) than at E12.5 (***Figure***
263 ***1D***). In contrast, G_{Nap} was similar at E14.5 (0.13 ± 0.14 nS, n = 10; N = 10) and E12.5 **(*Figure***
264 ***1E***). We also found that the G_{Nap} / G_{Kdr} ratio was significantly lower for SS V1^R recorded at
265 E14.5 (0.012 ± 0.004, n = 10) compared to RS V1^R (0.154 ± 0.022, n = 8) and PP V1^R (0.66 ±
266 0.132, n = 6) recorded at E12.5 (***Figure 1F***).
267 We tested the effect of 4-AP in SS V1^R at E14.5. At this embryonic age, 300 μM 4-AP
268 inhibited only 59.2% of I_{Kdr}. Increasing 4-AP concentration to 600 μM did not inhibit I_{Kdr}
269 significantly more (60.2%) (***Figure 6—figure supplement 2***), indicating that inhibition of I_{Kdr}
270 by 4-AP reached a plateau at around 300 μM. 600 μM 4-AP application had no significant

271 effect on I_A (***Figure 6—figure supplement 2***). The application of the maximal concentration
272 of 4-AP tested (600 μM) converted SS V1^R (n = 13; N = 13) to PP V1^R (23.1%; ***Figure 6A1,B***),
273 RS V1^R (38.5%; ***Figure 6A2,B***) or ME V1^R (38.4%; ***Figure 6B***), as was observed at E12.5, thus
274 indicating that the firing pattern of V1^R depends on the balance between I_{Nap} and
275 I_{Kdr} also at E14.5. Plateau potential and repetitive spiking recorded in the presence of 4-AP
276 at E14.5 were fully blocked by 0.5-1 μM TTX indicating that they were generated by voltage-
277 gated sodium channels (***Figure 6A1,A2***), as observed at E12.5.
278
279 **Theoretical analysis: the basic model**
280 As shown in ***Figure 7A*** for 26 cells, in which both G_{Nap} and G_{Kdr} were measured, the three
281 largest clusters revealed by the hierarchical clustering analysis (SS, RS and PP, which account
282 together for the discharge of more than 95% of cells, see ***Figure 5***) correspond to well
283 defined regions of the G_{Nap} - G_{Kdr} plane. Single spiking is observed only when G_{Nap} is
284 smaller than 0.6 nS. For larger values of G_{Nap}, repetitive spiking occurs when G_{Kdr} is larger
285 than 3.5 nS, and V1^R display plateau potentials when G_{Kdr} is smaller than 3.5 nS. Mixed
286 events (ME, 4.5% of the 163 cells used in the cluster analysis), where plateaus and spiking
287 episodes alternate, are observed at the boundary of RS and PP clusters. This suggested to us
288 that a conductance-based model incorporating only the leak current, I_{Nat}, I_{Nap} and I_{Kdr} (see
289 Materials and Methods) could account for most experimental observations, the observed
290 zonation being explained in terms of bifurcations between the different stable states of the
291 model. Therefore, we first investigated a simplified version of the model without I_A and slow
292 inactivation of I_{Nap}.
293 A one-parameter bifurcation diagram of this "basic" model is shown in ***Figure 7B*** for two
294 values of G_{Kdr} (2.5 nS and 10 nS) and a constant injected current I = 20 pA. In both cases,

295 the steady-state membrane voltage (stable or unstable) and the peak and trough voltages of
296 stable and unstable periodic solutions are shown as the function of the maximal
297 conductance G_{Nap} of the I_{Nap} current, all other parameters being kept constant. For G_{Kdr} =
298 10 nS, the steady-state membrane voltage progressively increases (in gray) with G_{Nap}, but
299 repetitive spiking (in red, see voltage trace for G_{Nap} = 1.5 nS) is not achieved until G_{Nap}
300 reaches point SN_1, where a saddle node (SN) bifurcation of limit cycles occurs. This fits with
301 the experimental data, where a minimal value of G_{Nap} is required for repetitive spiking (see
302 also [25], and is in agreement with the known role of I_{Nap} in promoting repetitive discharge
303 [50, 51]. Below SN_1, the model responds to the onset of a current pulse by firing only one
304 spike before returning to quiescence (see voltage trace for G_{Nap}= 0.2 nS), or a few spikes
305 when close to SN_1 (not shown) before returning to quiescence. The quiescent state becomes
306 unstable through a subcritical Hopf bifurcation (HB) at point HB_1, with bistability between
307 quiescence and spiking occurring between SN_1 and HB_1 points. Repetitive firing persists
308 when G_{Nap} is increased further and eventually disappears at point SN_2. The firing rate does
309 not increase much throughout the RS range (***Figure 7—figure supplement 1C***), remaining
310 between 20.1 Hz (at SN_1) and 28.7 Hz (at SN_2). A stable plateau appears at point HB_2 through
311 a subcritical HB. The model is bistable between HB_2 and SN_2, with plateau and large
312 amplitude APs coexisting in this range.
313 The model behaves very differently when G_{Kdr} is reduced to 2.5 nS (gray-blue curve in
314 ***Figure 7B***). It exhibits a unique stable fixed point whatever the value of G_{Nap} is, and the
315 transition from quiescence to plateau is gradual as G_{Nap} is increased. No repetitive spiking is
316 ever observed. This indicates that the activity pattern is controlled not only by G_{Nap} but also
317 by G_{Kdr}. This is demonstrated further in ***Figure 7C***, where G_{Nap} was fixed at 1.2 nS while
318 G_{Kdr} was increased from 0 to 25 nS. The model exhibits a plateau potential until G_{Kdr} is

increased past point the subcritical HB point HB_2, repetitive spiking sets in before at point SN_2 *via* a SN of limit cycles bifurcation. When G_{Kdr} is further increased, repetitive firing eventually disappears through a SN bifurcation of limit cycles at point SN_1, the quiescent state becomes stable through a subcritical HB at point HB_1, and bistability occurs between these two points. This behavior is in agreement with ***Figure 7A***.

Since both conductances G_{Nap} and G_{Kdr} control the firing pattern of embryonic $V1^R$ cells, we computed a two-parameters bifurcation diagram (***Figure 7D***), where the stability regions of the different possible activity states and the transition lines between them are plotted in the G_{Nap} - G_{Kdr} plane. The black curves correspond to the bifurcations HB_1 and HB_2 and delimit a region where only repetitive firing occurs. The red curves correspond to the SN bifurcations of periodic orbits associated with the transition from quiescence to firing (SN_1) and the transition from plateau to firing (SN_2). They encompass a region (shaded area) where repetitive firing can be achieved but may coexist with quiescence (between the HB_1 and SN_1 lines) or plateau potential (in the narrow region between the HB_2 and SN_2 lines).

Some important features of the diagram must be emphasized: 1) minimal values of both G_{Nap} (to ensure sufficient excitability) and G_{Kdr} (to ensure proper spike repolarization) are required for repetitive spiking, 2) quiescence and plateau can be clearly distinguished only when they are separated by a region of repetitive spiking (see also ***Figure 7B*** for G_{Kdr} = 10 nS), otherwise the transition is gradual (***Figure 7B*** for G_{Kdr}= 2.5 nS), 3) only oblique lines with an intermediate slope cross the bifurcation curve and enter the RS region (see, for example, the red line in ***Figure 7D***). This means that repetitive spiking requires an appropriate balance between I_{Nap} and I_{Kdr}. If the ratio G_{Nap}/G_{Kdr} is too large (blue line) or too small (gray line), only plateau potentials or quiescence will be observed at steady state. This is exactly what is observed in experiments, as shown by the cumulative distribution

343 function of the ratio G_{Nap}/G_{Kdr} for the different clusters of embryonic V1^R in ***Figure 7E***
344 (same cells as in ***Figure 7A***). The ratio increases according to the sequence SS → RS → ME →
345 PP, with an overlap of the distributions for SS V1^R and RS V1^R. Note also that the ratio for ME
346 cells (around 0.25) corresponds to the transition between repetitive spiking and plateau
347 potentials (more on this below).
348 Embryonic V1^R cells display voltage fluctuations that may exceed 5 mV and are presumably
349 due to channel noise. The relatively low number of sodium and potassium channels (of the
350 order of a few thousands) led to voltage fluctuations in the stochastic version of our model
351 comparable to those seen experimentally when the cell was quiescent (top voltage trace in
352 ***Figure 7D***) or when a voltage plateau occurred (bottom trace). Channel noise caused some
353 jitter during repetitive spiking (middle trace), and induced clearly visible variations in the
354 amplitude of APs. However, repetitive firing proved to be very robust and was not disrupted
355 by voltage fluctuations. Altogether, channel noise little alters the dynamics (compare the
356 deterministic voltage traces in ***Figure 7B*** and the noisy traces in ***Figure 7D***). This is likely
357 because channel noise has a broad power spectrum and displays no resonance with the
358 deterministic solutions of the model.
359 The one-parameter bifurcation diagram of the model was not substantially modified when
360 we took I_A into account, as shown in ***Figure 6—figure supplement 1***. It just elicited a slight
361 membrane hyperpolarization, an increase in the minimal value of G_{Nap} required for firing,
362 and a decrease of the firing frequency. The transition from repetitive firing to plateau was
363 not affected because I_A is then inactivated by depolarization.
364 The bifurcation diagram of ***Figure 7D*** accounts *qualitatively* for the physiological data on V1^R
365 at E12.5 presented in ***Figure 7A***, as shown in ***Figure 7F*** where the conductance data of
366 ***Figure 7A*** were superimposed on it. However, one must beware of making a more

367 *quantitative* comparison because the theoretical bifurcation diagram was established for a
368 constant injected current of 20 pA, whereas the current injected in experiments data varied
369 from neuron to neuron and ranged from 10 to 30 pA in the sample shown in ***Figure 7A***. The
370 position of bifurcation lines in the G_{Nap} - G_{Kdr} plane depends not only on the value of the
371 injected current, but on the values chosen for the other parameters, which also vary from
372 cell to cell but were kept at fixed values in the model (Ori et al. 2018). For instance, the
373 diagrams were computed in ***Figure 7D,F*** for G_{in}= 1 nS and C_{in}= 13 pF, the median values of
374 the input conductance and capacitance at E12.5, taking no account of the cell-to-cell
375 variations of these quantities. Between E12.5 and E14.5, C_{in} which provides an estimate of
376 the cell size, increases by 38% in average, whereas G_{in} is not significantly modified (see
377 ***Figure 4***). As illustrated in ***Figure 7G*** the two-parameters bifurcation diagram is then shifted
378 upward and rightward compared to ***Figure 7F***, because larger conductances are required to
379 obtain the same firing pattern. The observed regression of excitability from E12.5 to E14.5-
380 E15.5 (see ***Figure 4C***) thus comes from a decrease in G_{Nap} density (see presumable
381 developmental trajectories indicated by arrows in ***Figure 7F***) together with a shift of the RS
382 region as cell size increases. As a result, all 10 cells shown in ***Figure 7G*** are deeply inside the
383 SS region at E14.5.
384 It is less straightforward to explain on the basis of our model the experiments where 4-AP
385 changed the firing pattern of SS $V1^R$ (***Figure 2***). Indeed, the decrease of G_{Kdr} (***Figure 6—***
386 ***figure supplement 2***), although it may exceed 70% at the higher concentrations of 4-AP we
387 used, is not sufficient by itself to account for the change in the firing pattern of $V1^R$ (***Figure***
388 ***6—figure supplement 2***) because data points in the SS cluster will not cross the bifurcation
389 lines between SS and RS (SN1) and between RS and PP (SN2) when displaced downward in
390 the G_{Nap}- G_{Kdr} plane. However, 4-AP at a 300 μM concentration also decreases G_{in} (by 23%

391 in average and up to 50% in some neurons), the rheobase current with it, and the current
392 that was injected in cells during experiments was reduced accordingly. hen we take into
393 account this reduction of both G_{in} and I the two parameters bifurcation diagram pf the
394 model remains qualitatively the same, but it is shifted leftward and downward in the G_{Nap}-
395 G_{Kdr} plane (***Figure 6—figure supplement 2***). As a consequence, the bifurcation lines
396 between SS and RS and between RS and PP (SN2) are then successively crossed when G_{Kdr} is
397 reduced, in accordance with experimental results.
398
399 **Theoretical analysis: slow inactivation of $\mathbf{I_{Nap}}$ and bursting**
400 Our basic model accounts for the firing pattern of 73% of the 163 cells used in the cluster
401 analysis. However, bursting, under the form of recurring plateaus separated by brief
402 repolarization episodes (see a typical trace in ***Figure 8A left***), was experimentally observed in
403 half of PP $V1^R$ (24 out of 46), and plateaus intertwined with spiking episodes were recorded
404 in the 13 cells of the ME cluster (8% of the total sample, see ***Figure 8A right*** for a typical
405 example). Recurrent plateaus indicate membrane bistability and require that the $I - V$ curve
406 be S-shaped. This occurs when G_{Nap} is large and G_{Kdr} small. (***Figure 8B1,B2***). However, our
407 basic model lacks a mechanism for switching between quiescent state and plateau, even in
408 this case. Channel noise might induce such transitions, but our numerical simulations
409 showed that this is too infrequent to account for bursting (see voltage trace in ***Figure 8B1***
410 where the plateau state is maintained despite channel noise).
411 To explain recurrent plateaus during a constant current pulse, we have to incorporate in our
412 model an additional slow dynamical process. Therefore, we took into account the slow
413 inactivation of I_{Nap} that is observed in experiments. I_{Kdr} also inactivates slowly but over
414 times that are much longer than the timescale of bursting, which is why we did not take its

415 slow inactivation into account. The one-parameter bifurcation diagram of the basic model
416 without slow inactivation of I_{Nap} is shown in ***Figure 8C*** for G_{Kdr} = 5 nS and an injected
417 current reduced to 10 pA (as compared to 20 pA in the previous section), so as to allow for
418 bistability (see ***Figure 8B2***). The $G_{Nap} - V$ curve is then S-shaped, as shown in ***Figure 8B1***,
419 with a bistability region for G_{Nap} between 1.36 and 1.85 nS. This is in contrast with ***Figure 7B***
420 where the $G_{Nap} - V$ curve was monotonic. Adding the slow (de)inactivation of I_{Nap} then
421 caused periodic transitions between up (plateau) and down (quiescent) states, and the
422 model displayed a stable limit cycle (shown in black in ***Figure 8C***), as illustrated by the top
423 voltage trace on the right. This mechanism is known as pseudo-plateau or plateau-like
424 bursting (a.k.a. fold-subcritical HB bursting) [52]. It is akin to square wave bursting [53-56],
425 but the up-state is a stable fixed point rather than a limit cycle [57-59], which is why
426 recurrent plateaus are obtained rather than bursts of APs. The duration of the plateaus and
427 repolarization episodes depends on the values of G_{Nap} and G_{Kdr}. A voltage-independent
428 time constant $\tau_s = 2\ ms$ leads to up and down states of comparable durations (see top left
429 voltage trace in ***Figure 8C***). In agreement with the bifurcation diagram of ***Figure 8C***, the
430 persistent sodium current inactivates during plateaus (phase 1, see bottom right trace in in
431 ***Figure 8C***) and de-inactivates during quiescent episodes (phase 3, see bottom right trace).
432 Transitions from the down-state to the up-state occurs when inactivation has reached its
433 maximal value (phase 2) and transition from the up-state to the down state when it has
434 reached its maximum (phase 4).
435 Increasing G_{Nap} by 50% (or decreasing G_{Kdr}) makes plateaus much longer than quiescent
436 episodes (see top right voltage trace in ***Figure 8C***). This again points out to the fact that the
437 ratio is an important control parameter. Adding channel noise preserves bursting but
438 introduces substantial randomness in the duration of plateaus and repolarization episodes

439 (bottom right voltage trace in ***Figure 8C***). Moreover, it substantially decreases the duration
440 of both plateaus and quiescent episodes by making transition between the two states easier
441 (compare the two top voltage traces in ***Figure 8C***, both computed for $\tau_s = 2\,ms$). We also
442 noted that adding the I_A current lengthened the quiescence episodes (***Figure 6—figure***
443 ***supplement 1***).
444 Slow inactivation of I_{Nap} also provides an explanation for mixed patterns, where plateaus
445 alternate with spiking episodes (***Figure 8A, right***). They take place in our model near the
446 transition between repetitive spiking and plateau, as in experiments (see ***Figure 8A***). Slow
447 inactivation can lead to elliptic bursting, notably when the bifurcation HB_2 is subcritical [60,
448 61], which is the case here (***Figure 8D***). The model then displays a stable limit cycle with
449 alternating plateaus and spiking episodes, arising from crossing the bifurcation points HB_2
450 and SN_2 back and forth (see bifurcation diagram in ***Figure 8D*** and top voltage trace). We
451 note that sufficient de-inactivation of I_{Nap} for triggering a new plateau (phase 3 in the
452 bottom trace of ***Figure 8D***) may be difficult to achieve during spiking episodes, because
453 voltage oscillates over a large range, which tends to average out the variations of the
454 inactivation level. If de-inactivation is not sufficient, the model keeps on spiking repetitively
455 without returning to the plateau state. This is what occurs for cells well within the RS region,
456 far away from the RS-PP transition. It also probably explains why it was difficult in many
457 recorded cells to elicit plateaus by increasing the injected current, inactivation balancing
458 then the increase of I_{Nap} induced by the larger current.
459 Altogether, our study shows that a model incorporating the slow inactivation of
460 I_{Nap} accounts for all the firing patterns displayed by cells from the PP and ME clusters.
461

462 # Discussion

463 V1^R constitute a homogeneous population when referring to their transcription factor
464 program during development [24, 62], their physiological function [63] and their firing
465 pattern at postnatal stages [27]. Surprisingly, our electrophysiological recordings and our
466 cluster analysis clearly indicate that distinct functional classes of V1^R are transiently present
467 during development at the onset of the SNA (E11.5-E12.5). Five different groups of
468 embryonic V1^R were defined using cluster analysis, according to their firing properties.

469

470 **Development of the firing pattern of embryonic V1^R during SNA**

471 It is generally assumed that, during early development, newborn neurons cannot sustain
472 repetitive firing [35, 48]. Later on, neurons progressively acquire the ability to fire
473 repetitively, APs become sharper, and neurons eventually reach their mature firing pattern,
474 due to the progressive appearance of a panoply of voltage-gated channels with different
475 kinetics [18, 35, 48]. Our results challenge the general view that single spiking is a more
476 primitive form of excitability [35]. Indeed, we show that repetitive firing and plateau
477 potentials dominated at early stages (E11.5-E12.5), while single spiking was prevailing only
478 later (E13.5- E16.5).

479 The different V1^R firing patterns observed at E11.5-E12.5 might reflect variability in the
480 maturation level between V1^R at a given developmental stage, as suggested for developing
481 MNs [64, 65]. However, this is unlikely since V1^R transiently lose their ability to sustain tonic
482 firing or plateau potential after E13.5. The heterogeneous discharge patterns of V1^R
483 observed before E13.5 contrasts with the unique firing pattern of V1^R at postnatal age [27].
484 Accordingly, the transient functional heterogeneity of V1^R rather reflects an early initial
485 developmental stage (E11.5-E13.5) of intrinsic excitability.

486 The physiological meaning of the transient functional involution of $V1^R$ that follows, after
487 E12.5, is puzzling. To our knowledge, such a phenomenon was never described in
488 vertebrates during CNS development. So far, a functional involution was described only for
489 inner hair cells between E16 and P12 [66, 67] and cultured oligodendrocytes [68], and it was
490 irreversible. Because most $V1^R$ cannot sustain tonic firing after E12.5, it is likely that their
491 participation to SNA is limited to the developmental period before other GABAergic
492 interneuron subtypes mature and start to produce GABA and glycine [69]. Interestingly,
493 embryonic $V1^R$ begin to recover their capability to sustain tonic firing when locomotor-like
494 activity emerges [4, 11], a few days before they form their recurrent synaptic loop with MNs
495 (around E18.5 in the mouse embryos, [70]). One possible function of the transient involution
496 between E12.5 and E15.5 could be to regulate the growth of $V1^R$ axons toward their targets.
497 It is indeed known that low calcium fluctuations within growth cones are required for axon
498 growth while high calcium fluctuations stop axon growth and promote growth cone
499 differentiation [71].
500

501 **Ion channels mechanisms underlying the functional heterogeneity of embryonic $V1^R$**

502 Blockade of I_{Nap} leads to single spiking [25], which emphasizes the importance of this
503 current for the occurrence of repetitive firing and plateau potentials in $V1^R$ at early
504 developmental stages. But these neurons can also switch from one firing pattern to another,
505 when G_{Kdr} is decreased by 4-AP, which emphasizes the importance of I_{Kdr}. We found that
506 the main determinant of embryonic $V1^R$ firing pattern is the balance between G_{Nap} and G_{Kdr}.
507 A Hodgkin-Huxley-type model incorporating a persistent sodium current I_{Nap} provided a
508 parsimonious explanation of all the firing patterns recorded in the $V1^R$ population at E12.5. It
509 provided a mathematical interpretation for the clustering of embryonic $V1^R$ shown by the

510 hierarchical analysis and accounted for the effect of 4-AP and riluzole [25] on the discharge.
511 Remarkably, it highlighted how a simple mechanism involving only the two opposing
512 currents I_{Nap} and I_{Kdr} , but not I_A, could produce functional diversity in a population of
513 developing neurons. The model explained why minimal G_{Nap} and G_{Kdr} are required for firing,
514 and how a synergy between G_{Nap} and G_{Kdr} controls the firing pattern and accounts for the
515 zonation of the $G_{Nap} - G_{Kdr}$ plane that is observed experimentally.
516 Taking into account the slow inactivation of I_{Nap} to the model allowed us to explain the
517 bursting patterns displayed by cells of the PP and ME clusters. We showed, in particular, that
518 mixed events arose from elliptic bursting at the repetitive spiking-plateau transition and that
519 smooth repetitive plateaus could be explained by a pseudo-plateau bursting mechanism [52,
520 58]. Such bursting scenario has been previously studied in models of endocrine cells [57, 72,
521 73] and adult neurons [74], but rarely observed in experiments.
522 Heterogeneity of the discharge pattern of pacemaker neurons has also been observed in the
523 embryonic pre-Bötzinger network [75]. However, it was related there to the gradual change
524 of balance between two inward currents, I_{Nap} and the calcium-activated nonselective
525 cationic current I_{CAN} during neuronal maturation, which led to the progressive replacement
526 of pseudo-plateau bursting by elliptic bursting. Such a scenario cannot account for the
527 variety of discharge patterns observed in embryonic $V1^R$ at the E11.5-12.5 stage of
528 development [25]. Our theoretical analysis and our experimental data clearly indicate that
529 the interplay between two opposing currents is necessary to explain all the firing patterns of
530 $V1^R$. Our model is of course not restricted to embryonic $V1^R$, but may also apply to any
531 electrically compact cell, the firing activity of which is dominated by I_{Nap} and delayed
532 rectifier potassium currents. This is the case of many classes of embryonic cells in mammals

533 at an early stage of their development. It can also apply to the axon initial segment, where
534 G_{Nap} and G_{Kdr} are known to play the major role in the occurrence of repetitive firing [76].
535 Altogether our experimental and theoretical results provide a global view of the
536 developmental trajectories of embryonic V1^R (see ***Figure 7F,G***). At E12.5, conductances of
537 embryonic V1^R are widely spread in the $G_{Nap} - G_{Kdr}$ plane, which explains the
538 heterogeneity of their firing patterns. This likely results from the random and uncorrelated
539 expression of sodium and potassium channels from cell to cell at this early stage. Between
540 E12.5 and E14.5-15.5 cell size increases, and G_{Kdr} with it, while the density of sodium
541 channels decreases (see ***Figure 1*** **and** ***4***). The functional involution displayed by V1^R between
542 E12.5 and E15.5 thus mainly results from a decrease of G_{Nap} coordinated with an increase of
543 G_{Kdr}. How these synergistic processes are controlled during this developmental period
544 remains an open issue.
545 It is important to note that the presence of I_{Nap} is required for the functional diversity of V1^R.
546 Indeed, in the absence of I_{Nap}, V1^R lose their ability to generate plateau potentials or to fire
547 repetitively. More generally, when the diversity of voltage-gated channels is limited, as
548 observed in embryonic neurons [18], changes in the balance between I_{Kdr} and non (or
549 poorly) inactivating inward current can modify the firing pattern. This can be achieved not
550 only by I_{Nap}, but also by other slowly or non-inactivating inward conductances, such as I_{CAN}
551 [75]. Our work also clearly indicates that a change in the firing pattern can only occur if a
552 change in inward conductances cannot be counterbalanced by a corresponding change in
553 outward conductances. This implies that there is no homeostatic regulation of channel
554 density to ensure the robustness of V1^R excitability during its early development, contrarily
555 to the mature CNS [37]. In addition, the poor repertoire of voltage-gated channels at this

556 developmental stage precludes channel degeneracy, which is also known to ensure the
557 robustness of excitability in mature neurons [37].
558 In conclusion, our results demonstrate that a simple mechanism involving only two slowly
559 inactivating voltage-gated channels with opposite effects is sufficient to produce functional
560 diversity in immature neurons having a limited repertoire of voltage-gated channels.
561

562 # Materials and Methods

563 **Isolated spinal cord preparation**

564 Experiments were performed in accordance with European Community guiding principles on
565 the care and use of animals (86/609/CEE, CE Off J no. L358, 18 December 1986), French
566 decree no. 97/748 of October 19, 1987 (J Off République Française, 20 October 1987, pp.
567 12245-12248). All procedures were carried out in accordance with the local ethics
568 committee of local Universities and recommendations from the CNRS. We used GAD67eGFP
569 knock-in mice to visualize putative GABAergic INs [77], as in our previous study [25]. To
570 obtain E12.5-E16.5 transgenic GAD67-eGFP embryos, 8 to 12 weeks old wild-type Swiss
571 female mice were crossed with GAD67-eGFP Swiss male mice.
572 Isolated mouse SCs from 420 embryos were used in this work and obtained as previously
573 described [28, 78]. Briefly, pregnant mice were anesthetized by intramuscular injection of a
574 mix of ketamine and xylazine and sacrificed using a lethal dose of CO_2 after embryos of
575 either sex were removed. Whole SCs were isolated from eGFP-positive embryos and
576 maintained in an artificial cerebrospinal fluid (ACSF) containing 135 mM NaCl, 25 mM
577 $NaHCO_3$, 1 mM NaH_2PO_4, 3 mM KCl, 11 mM glucose, 2 mM $CaCl_2$, and 1 mM $MgCl_2$ (307
578 mOsm/kg H_2O), continuously bubbled with a 95% O_2-5% CO_2 gas mixture.

579 In the lumbar SC of GAD67eGFP mouse embryos, eGFP neurons were detected using 488 nm
580 UV light. They were localized in the ventro-lateral marginal zone between the motor
581 columns and the ventral funiculi [62]. Embryonic $V1^R$ identity was confirmed by the
582 expression of the forkhead transcription factor Foxd3 [25].
583
584 **Whole-cell recordings and analysis**
585 The isolated SC was placed in a recording chamber and was continuously perfused (2 ml/min)
586 at room temperature (22-26°C) with oxygenated ACSF. Whole-cell patch-clamp recordings of
587 lumbar spinal embryonic $V1^R$ were carried out under direct visualization using an infrared-
588 sensitive CCD video camera. Whole-cell patch-clamp electrodes with a resistance of 4-7 MΩ
589 were pulled from thick-wall borosilicate glass using a P-97 horizontal puller (Sutter
590 Instrument Co., USA). They were filled with a solution containing (in mM): 96.4 K
591 methanesulfonate, 33.6 KCl, 4 $MgCl_2$, 4 Na_2ATP, 0.3 Na_3GTP, 10 EGTA, and 10 HEPES (pH 7.2;
592 290 mOsm/kg-H_2O). This intracellular solution led to an equilibrium potential of chloride ions,
593 E_{Cl}, of about -30 mV, close to the physiological values measured at E12.5 in spinal MNs [28].
594 The junction potential (6.6 mV) was systematically corrected offline.
595 Signals were recorded using Multiclamp 700B amplifiers (Molecular Devices, USA). Data
596 were low-pass filtered (2 kHz), digitized (20 kHz) online using Digidata 1440A or 1550B
597 interfaces and acquired using pCLAMP 10.5 software (Molecular Devices, USA). Analyses
598 were performed off-line using pCLAMP 10.5 and Axograph 1.7.2 (Molecular devices;
599 RRID:SCR_014284) software packages.
600 In voltage-clamp mode, voltage-dependent K^+ currents (I_{Kv}) were elicited in the presence of
601 1 μM TTX by 500 ms depolarizing voltage steps (10 mV increments, 10 s interval) after a
602 prepulse of 300 ms at V_H = -100 mV. To isolate I_{Kdr}, voltage steps were applied after a 300

603 ms prepulse at V_H = -30 mV that inactivated the low threshold transient potassium current
604 I_A. I_A was then obtained by subtracting offline I_{Kdr} from the total potassium current I_{Kv}.
605 Capacitance and leak current were subtracted using on-line P/4 protocol provided by
606 pCLAMP 10.5.
607 In current-clamp mode, $V1^R$ discharge was elicited using 2 s depolarizing current steps (from
608 0 to ≈ 50 pA in 5-10 pA increments, depending on the input resistance of the cell) with an 8 s
609 interval to ensure that the membrane potential returned to V_H. When a cell generated a
610 sustained discharge, the intensity of the depolarizing pulse was reduced to the minimal
611 value compatible with repetitive firing.
612 I_{Nap} was measured in voltage-clamp mode using a 70 mV/s depolarizing voltage ramp [79].
613 This speed was slow enough to preclude substantial contamination by the inactivating
614 transient current and fast enough to avoid substantial inactivation of I_{Nap}. Subtraction of
615 the current evoked by the voltage ramp in the presence of 1 μM tetrodotoxin (TTX) from the
616 control voltage ramp-evoked current revealed I_{Nap}.
617
618
619 **Pharmacological reagents**
620 During patch-clamp recordings, bath application of TTX (1 μM, Alomone, Israel) or 4-AP (0.3 -
621 600 μM, Sigma) was done using 0.5 mm diameter quartz tubing positioned, under direct
622 visual control, 50 μm away from the recording area. The quartz tubing was connected to 6
623 solenoid valves linked with 6 reservoirs *via* a manifold. Solutions were gravity-fed into the
624 quartz tubing. Their application was controlled using a VC-8 valve controller (Warner
625 Instruments, USA).

626 4-aminopyridine (4-AP; Sigma Aldrich, USA) was used to block I_{Kdr}. To determine the
627 concentration–response curve, $I - V$ curves of I_{Kdr} for different concentrations of 4-AP (0.3
628 to 300 μM) were compared to the control curve obtained in the absence of 4-AP. The
629 percentage of inhibition for a given concentration was calculated by dividing the peak
630 intensity of I_{Kdr} by the peak value obtained in control condition. The obtained normalized
631 concentration–response curves were fitted using the Hill equation:

632 $$\frac{100-I_{min}}{1+([4-AP]/IC_{50})^{n_H}} + I_{min} ,$$

633 where [4-AP] is the 4-AP concentration, I_{min} is the residual current (in percentage of the
634 peak I_{Kdr}), $100 - I_{min}$ is the maximal inhibition achieved for saturating concentration of 4-
635 AP, IC_{50} is the 4-AP concentration producing half of the maximal inhibition, and n_H is the
636 Hill coefficient. Curve fitting was performed using KaleidaGraph 4.5 (Synergy Software, USA).
637

638 **Immunohistochemistry and confocal microscopy**

639 E14.5 embryos were collected from pregnant females. Once dissected out of their yolk sac,
640 SCs were dissected and immediately immersion-fixed in phosphate buffer (PB 0.1 M)
641 containing 4% paraformaldehyde (PFA; freshly prepared in PB, pH 7.4) for 1 h at 4°C. Whole
642 SCs were then rinsed out in 0.12 M PB at 4°C, thawed at room temperature, washed in PBS,
643 incubated in NH_4Cl (50 mM), diluted in PBS for 20 min and then permeabilized for 30 min in
644 a blocking solution (10% goat serum in PBS) with 0.2% Triton X-100. They were incubated for
645 48 h at 4°C in the presence of the following primary antibodies: guinea pig anti-FoxD3
646 (1:5000, gift from Carmen Birchmeier and Thomas Müller of the Max Delbrück Center for
647 Molecular Medicine in Berlin) and rabbit anti-cleaved Caspase-3 (1:1000, Cell Signaling
648 Technology Cat# 9661, RRID:AB_2341188). SCs were then washed in PBS and incubated for 2
649 h at RT with secondary fluorescent antibodies (goat anti-rabbit-conjugated 649; donkey anti-

650 guinea pig-conjugated Alexa Fluor 405 [1:1000, ThermoFisher]) diluted in 0.2% Triton X-100
651 blocking solution. After washing in PBS, SCs were dried and mounted in Mowiol medium
652 (Millipore, Molsheim, France). Preparations were then imaged using a Leica SP5 confocal
653 microscope. Immunostaining was observed using a 40X oil-immersion objective with a
654 numerical aperture of 1.25, as well as with a 63X oil-immersion objective with a numerical
655 aperture of 1.32. Serial optical sections were obtained with a Z-step of 1 µm (40X) and 0.2-
656 0.3 µm (63X). Images (1024x1024; 12-bit color scale) were stored using Leica software LAS-
657 AF and analyzed using ImageJ 1.5 (N.I.H., USA; http//rsb.info.nih.gov/ij/) and Adobe
658 Photoshop CS6 (Adobe, USA) software.
659
660 **Cluster analysis**
661 To classify the firing patterns of embryonic $V1^R$, we performed a hierarchical cluster analysis
662 on a population of 163 cells. Each cell was characterized by three quantitative measures of
663 its firing pattern (see legend of Figure 5). After normalizing these quantities to zero mean
664 and unit variance, we performed a hierarchical cluster analysis using the hclust function in R
665 software (version 3.3.2, https://cran.r-project.org/) that implements the complete linkage
666 method. The intercluster distance was defined as the maximum Euclidean distance between
667 the points of two clusters, and, at each step of the process, the two closest clusters were
668 merged into a single one, thus constructing progressively a dendrogram. Clusters were then
669 displayed in data space using the dendromat function in the R package 'squash' dedicated to
670 color-based visualization of multivariate data. The best clustering was determined using the
671 silhouette measure of clustering consistency [80]. The silhouette of a data point, based on
672 the comparison of its distance to other points in the same cluster and to points in the closest
673 cluster, ranges from -1 to 1. A value near 1 indicates that the point is well assigned to its

674 cluster, a value near 0 indicates that it is close to the decision boundary between two
675 neighboring clusters, and negative values may indicate incorrect assignment to the cluster.
676 This allowed us to identify an optimal number k of clusters by maximizing the overall
677 average silhouette over a range of possible values for k [80], using the silhouette function in
678 the R package 'cluster'.
679
680 **Biophysical modeling**
681 To understand the relationship between the voltage-dependent membrane conductances
682 and the firing patterns of embryonic V1^R, we relied on a single compartment conductance-
683 based model that included the leak current, the transient and persistent components of the
684 sodium current, I_{Nat} and I_{Nap}, a delayed rectifier potassium current I_{Kdr} and the
685 inactivating potassium current I_A revealed by experiments. Voltage evolution then followed
686 the equation
687 $C_{in}\frac{dV}{dt} = G_{in}(V_r - V) + G_{Nat}m^3h(E_{Na} - V) + G_{Nap}m_p^3s(V_{Na} - V) + G_{Kdr}n^3(E_K - V) +$
688 $G_A m_A h_A(E_K - V) + I$ (1),
689 ,
690 where C_{in} was the input capacitance; G_{in} the input conductance; G_{Nat}, G_{Nap}, G_{Kdr} and
691 G_A the maximal conductances of the aforementioned currents; m, m_p, n and m_A their
692 activation variables; h the inactivation variable of I_{Nat}, s the slow inactivation variable of
693 I_{Nap}, and m_A the inactivation variable of I_A. V_r is the baseline potential imposed by *ad hoc*
694 current injection in current-clamp experiments; E_{Na} and E_K are the Nernst potentials of
695 sodium and potassium ions, and I the injected current. All gating variables satisfied
696 equations of the form:
697 $\tau_x\frac{dx}{dt} = x_\infty(V) - x,$

where the (in)activation curves were modeled by a sigmoid function of the form:

$$x_\infty = \frac{1}{1+\exp\left(-(V-V_{x)}/k_x\right)}$$

with k_x being positive for activation and negative for inactivation. The time constant τ_x was voltage-independent except for the inactivation variables h and s. The activation variable m_A of I_A was assumed to follow instantaneously voltage changes.

The effect of channel noise was investigated with a stochastic realization of the model, where channels kinetics were described by Markov-type models, assuming a unitary channel conductance of 10 pS for all channels.

Choice of model parameters

Most model parameters were chosen on the basis of experimental measurements performed in the present study or already reported [25]. Parameters that could not be constrained from our experimental data were chosen from an experimentally realistic range of values. V_r was set at -60 mV as in experiments (see ***table 1***). C_{in} (average 13.15 pF, 50% between 11.9 and 15.1 pF, only 18 cells out of 246 in the first quartile below 7.2 pF or in the fourth quartile above 19 pF) and G_{in} (50% of cells between 0.71 and 1.18 nS, only 7 out of 242 with input conductance above 2 nS) were not spread much in the cells recorded at E12.5, which showed that most embryonic $V1^R$ were of comparable size. Interestingly, C_{in} and G_{in} were not correlated, which indicated that the input conductance was determined by the density of leak channels rather than by the sheer size of the cell. Moreover, no correlation was observed between the passive properties and the firing pattern [25]. Therefore, we always set G_{in} and C_{in} to 1 nS and 13 pF in the model (except in ***Figure 6—figure supplement 2***), close to the experimental medians (0.96 nS and 13.15 pF, respectively). The

721 membrane time constant C_{in}/G_{in} was then equal to 13 ms, which was also close to the
722 experimental median (13.9 ms, N=241).
723 E_{Na} was set to 60 mV (see [25]). The activation curve of I_{Nap} was obtained by fitting
724 experimental data, leading to an average mid-activation of -36 mV and an average steepness
725 of 9.5 mV. The experimentally measured values of G_{Nap} were in the range 0-2.2 nS. We
726 assumed that the activation curve of I_{Nat} was shifted rightward by 10 mV in comparison to
727 I_{Nap}. No experimental data was available for the inactivation of I_{Nat}. We chose a mid-
728 inactivation voltage V_h= -45 mV and a steepness k_h=-5 mV. We also assumed that the
729 activation time constant of both I_{Nat} and I_{Nap} was 1.5 ms, and that the inactivation time
730 constant was voltage-dependent: $\tau_h(V) = 16.5 - 13.5\tanh((V+20)/15)$, decreasing by
731 one order of magnitude (from 30 ms down to 3 ms) with the voltage increase. This enabled
732 us to account for the shape of the action potentials recorded in experiments, showing a slow
733 rise time and rather long duration. The conductance G_{Nat} was not measured experimentally.
734 When choosing a reasonable value of 20 nS for G_{Nat}, the model behaved very much as
735 recorded embryonic V1^R: with similar current threshold (typically 10-20 pA) and stable
736 plateau potential obtained for the largest values of G_{Nap}.
737 When taking into account slow inactivation of I_{Nap} (see ***Figure 8***), we chose V_s = -30 mV for
738 the mid-inactivation voltage and set the steepness k_s at -5 mV (as for the inactivation of
739 I_{Nat}). For simplicity, we assumed that the inactivation time constant was voltage-
740 independent and set it at a value of 2 s.
741 E_K was set to the experimentally measured value of -96 mV [25]. The activation parameters
742 of I_{Kdr} were obtained by fitting the experimental data: V_n = -20 mV, k_n = 15 mV, τ_n = 10 ms
743 and an activation exponent of 3. The activation and inactivation properties of I_A were also
744 chosen based on experimental measurements. Accordingly, V_{m_A} = -30 mV, k_{m_A} = -12 mV,

745 V_{h_A} = -70 mV, k_{h_A} = -7 mV, and τ_{h_A}= 23 ms. When I_A was taken into account, we assumed
746 that $G_A = G_{Kdr}$, consistently with experimental data (see ***Figure 6—figure supplement 1***).
747

748 **Numerical simulations and dynamical systems analysis**

749 We integrated numerically the deterministic model using the freeware XPPAUT [81] and a
750 standard fourth-order Runge-Kutta algorithm. XPPAUT was also used to compute one-
751 parameter and two-parameters bifurcation diagrams. The stochastic version of the model
752 was also implemented in XPPAUT and computed with a Gillespie's algorithm [82].
753 To investigate the dynamics of the model with slow inactivation of I_{Nap}, we relied on
754 numerical simulations together with fast/slow dynamics analysis [83]. In this approach, one
755 distinguishes slow dynamical variables (here only s) and fast dynamical variables. Slow
756 variables vary little at the time scale of fast variables and may therefore be considered as
757 constant parameters of the fast dynamics in first approximation. In contrast, slow variables
758 are essentially sensitive to the time average of the fast variables, much more than to their
759 instantaneous values. This separation of time scales allows one to conduct a phase plane
760 analysis of the full dynamics.
761

762 **Statistics**

763 Samples sizes (n) were determined based on previous experience. The number of embryos
764 (N) is indicated in the main text and figure captions. No power analysis was employed, but
765 sample sizes are comparable to those typically used in the field. All values were expressed as
766 mean with standard error of mean (SEM). Statistical significance was assessed by non-
767 parametric Kruskal-Wallis test with Dunn's post hoc test for multiple comparisons, Mann-
768 Whitney test for unpaired data or Wilcoxon matched pairs test for paired data using

769 GraphPad Prism 7.0e Software (USA). Significant changes in the proportions of firing
770 patterns with age were assessed by chi-square test for large sample and by Fisher's exact
771 test for small sample using GraphPad Prism 7.0e Software. Significance was determined as
772 $p<0.05$ (*), $p<0.01$ (**) or $p<0.001$ (***). The exact p value was mentioned in the result
773 section or in the figure captions.

774 ## Acknowledgments

775 We thank Susanne Bolte, Jean-François Gilles and France Lam for assistance with confocal
776 imaging (IBPS imaging facility) and IBPS rodent facility team for animal care and production.
777 We thank University Paris Descartes for hosting Yulia Timofeeva as an invited professor. This
778 work was supported by INSERM, CNRS, Sorbonne Université (Paris), Université de Bordeaux,
779 Université Paris Descartes and Fondation pour la Recherche Médicale.

780

781 ## Additional information

782 **Competing interests**

783 The authors declare no competing interests

784

785 ## Figure captions

786 **Figure 1. G_{Kdr} and G_{Nap} in embryonic $V1^R$ at E12.5 and E14.5**

787 (A) Representative traces of voltage responses showing single-spiking activity in E12.5 SS
788 $V1^R$ (A1), repetitive action potential firing in RS $V1^R$ (A2), Mixed of plateau potential activity
789 and repetitive action potential firing in ME $V1^R$ (A3) and plateau potential activity in PP $V1^R$
790 (A4). (B) Representative examples of the total outward K^+ currents (IKv total) obtained
791 from V_H = -100 mV (left traces), of I_{Kdr} (V_H = -30 mV, middle traces) and of isolated I_A (left
792 traces) recorded at E12.5 in SS $V1^R$ (B1), RS $V1^R$ (B2), ME $V1^R$ (B3) and PP $V1^R$ (B4). Voltage-
793 dependent potassium currents were evoked in response to 10 mV membrane potential steps
794 (200 ms) from -100 or from -30 mV to +40 mV (10 s interval between pulses). $V1^R$ were
795 voltage clamped at V_H = -60 mV. A prepulse of -40 mV (300 ms) was applied to activate both
796 I_A and I_{Kdr}. I_{Kdr} was isolated by applying a prepulse of 30 mV (300 ms) to inactivate I_A (B1

797 insert). I_A was isolated by subtracting step-by-step the currents obtained using a pre-pulse of
798 30 mV (V_H = - 30 mV) from the currents obtained using a pre-pulse of -40 mV (V_H = -100 mV).
799 (C) Current-voltage relationship ($I - V$ curves) of I_{Kdr} (filled circles) and of I_A (open circles)
800 recorded in SS V1^R (C1), RS V1^R (C2), ME V1^R (C3) and PP V1^R (C4). $I - V$ curves were
801 obtained from currents shown in B1, B2, B3 and B4. Note that $I - V$ curves are similar
802 between SS V1^R, RS V1^R, ME V1^R and PP V1^R. (D) Bar graph showing maximal G_{Kdr} value
803 (Max G_{Kdr}) in SS V1^R at E12.5 (n = 9; N = 9; gray bar) and at E14.5 (n = 10; N = 10 gray bar),
804 and in RS V1^R (n = 7; N = 7; red bar), ME V1^R (n = 3; N = 3 purple bar) and PP V1^R at E12.5 (n =
805 7; N = 7 blue bar). G_{Kdr} was calculated from I_{Kdr} at V_H = + 20 mV, assuming a K^+ equilibrium
806 potential of -96 mV. There is no significant difference in G_{Kdr} between SS V1^R and RS V1^R,
807 while G_{Kdr} is significantly smaller in PP V1^R as compared to SS V1^R and RS V1^R. G_{Kdr} was
808 significantly higher in SS V1^R at E14.5 than in SS V1^R, RS V1^R and PP V1^R at E12.5. (Kruskall-
809 Wallis test P < 0.0001; SS V1^R versus RS V1^R at E12.5, P = 0.5864; SS V1^R versus PP V1^R at
810 E12.5, P = 0.0243; RS V1^R versus PP V1^R at E12.5, P = 0.0086; E14.5 SS V1^R versus E12.5 SS V1^R,
811 P = 0.0048; E14.5 SS V1^R versus E12.5 RS V1^R, P = 0.0384, E14.5 SS V1^R versus E12.5 PP V1^R, P
812 < 0.0001). The increase in G_{Kdr} between E12.5 and E14.5 is likely to be due to the increase in
813 neuronal size (input capacitance; Figure 2A). Indeed, there was no significant difference
814 (Mann Whitney test, P = 0.133) in G_{Kdr} density between SS V1^R at E12.5 (n = 9; N = 9 gray
815 bar) and at E14.5 (n = 10; N = 10 gray bar). (E) Bar graph showing the maximal G_{Nap} value
816 (Max G_{Nap}) in SS V1^R at E12.5 (n = 9; N = 9 gray bar) and E14.5 (n = 10; N = 10 gray bar), and
817 in RS V1^R (n = 8; N = 8 red bar), ME V1^R (n = 3; N = 3 purple bar) and PP V1^R (n = 6; N = 6 blue
818 bar) at E12.5. Max G_{Nap} was calculated from maximal I_{Nap} value measured on current
819 evoked by assuming a Na^+ equilibrium potential of +60 mV. There was no difference
820 in G_{Nap} between RS V1^R and PP V1^R. On the contrary, G_{Nap} measured in SS V1^R at E12.5 or at

821 E14.5 was significantly smaller as compared to G_{Nap} measured at E12.5 in RS V1^R or in PP
822 V1^R. G_{Nap} measured at E12.5 and E14.5 in SS V1^R were not significantly different (Kruskall-
823 Wallis test $P < 0.0001$; E12.5 SS V1^R versus E12.5 RS V1^R, $P = 0.0034$; E12.5 SS V1^R versus
824 E12.5 PP V1^R, $P = 0.0006$; E12.5 RS V1^R versus E12.5 PP V1^R, $P = 0.5494$; E14.5 SS V1^R versus
825 E12.5 SS V1^R, $P = 0.5896$; E14.5 SS V1^R versus E12.5 RS V1^R, $P = 0.0005$; E14.5 SS V1^R versus
826 E12.5 PP V1^R, $P < 0.0001$). (F) Histograms showing the G_{Nap} / G_{Kdr} ratio in SS V1^R at E12.5 (n
827 = 9; gray bar) and E14.5 (n = 10; green bar) and in RS V1^R (n = 8; red bar), ME V1^R (n = 3;
828 purple bar) and PP V1^R (n = 6; blue bar) at E12.5. Note that the G_{Nap} / G_{Kdr} ratio differs
829 significantly between SS V1^R, RS V1^R and PP V1^R at E12.5, while it is not different between SS
830 V1^R recorded at E12.5 and at E14.5 (Kruskall-Wallis test $P < 0.0001$; SS V1^R versus RS V1^R at
831 E12.5, $P = 0.0367$; SS V1^R versus PP V1^R at E12.5, $P < 0.0001$; RS V1^R versus PP V1^R at E12.5, P
832 = 0.0159; E14.5 SS V1^R versus E12.5 SS V1^R, $P = 0.2319$; E14.5 SS V1^R versus E12.5 RS V1^R, P =
833 0.0017; E14.5 SS V1^R versus E12.5 PP V1^R $P < 0.0001$). Data shown in A and B were used to
834 calculate G_{Nap} / G_{Kdr} ratio shown in C. (*$P < 0.05$, ** $P < 0.01$, *** $P < 0.001$).
835
836 **Figure 2. Increasing 4-AP concentration changed the firing pattern of single spiking**
837 **embryonic V1^R recorded at E12.5**
838 The firing pattern of embryonic V1^R was evoked by 2 s suprathreshold depolarizing current
839 steps. (A) Representative traces showing examples of the effect of increasing concentration
840 of 4-AP (from 3 to 300 µM) on the firing pattern of a SS V1^R recorded at E12.5. Note that in
841 A1, increasing 4-AP concentration converted single spiking (gray trace) to repetitive spiking
842 (red trace), repetitive spiking to a mixed event pattern (purple trace) and mixed events to
843 plateau potential (blue trace). (A2) Example of SS V1^R in which increasing 4-AP concentration
844 converted single spiking to repetitive spiking only. (A3) Bar plots showing the change in the

845 firing pattern of SS $V1^R$ according to 4-AP concentrations (control n = 10; N = 10, 3 µM 4-AP n
846 = 8; N = 8, 10 µM 4-AP n = 10; N = 10, 30 µM 4-AP n = 10; N = 10, 100 µM 4-AP n = 10; N = 10,
847 300 µM 4-AP n = 8; N = 8). (B) Representative traces showing the effect of 0.5 µM TTX on a
848 plateau potential evoked in a SS $V1^R$ in the presence of 300 µM 4-AP. (C) Representative
849 traces showing the effect of 0.5 µM TTX on repetitive AP firing evoked in a SS $V1^R$ in the
850 presence of 300 µM 4-AP. In both cases, the application of TTX fully blocked the responses
851 evoked in the presence of 4-AP, indicating that they were underlain by the activation of
852 voltage-gated Na^+ channels.
853
854 **Figure 3. Cluster analysis of $V1^R$ firing pattern at E12.5**
855 (A, inserts) Cluster analysis of embryonic $V1^R$ firing pattern was performed using three
856 parameters that describe the firing pattern during a 2 s suprathreshold depolarizing pulses:
857 the mean of the half-amplitude event duration (mean ½Ad), the coefficient of variation of ½
858 Ad (CV ½Ad) allowing to quantify the AP variation within a train (CV was set to 0 when the
859 number of spikes evoked by a depolarizing pulse was ≤ 3) and the duration ratio ddr = Σ½
860 Ad/Pw, obtained by dividing the sum of ½ Ad by the pulse duration Pw, that indicates the
861 total time spent in the depolarized state. For example, ddr = 1 when a plateau potential lasts
862 as long as the depolarizing pulse. Conversely, its value is low when the depolarizing pulse
863 evokes a single AP only. (A) Dendrogram for complete linkage hierarchical clustering of 164
864 embryonic $V1^R$ (N = 140) according to the values of log mean ½Ad, of CV ½Ad and of log ddr.
865 The colored matrix below the dendrogram shows the variations of these three parameters
866 for all the cells in the clusters (colored trees) extracted from the dendrogram. (B) The
867 number of clusters was determined by analyzing the distribution of silhouette width values
868 (see Material and Methods). The boxplots show the distribution of silhouette width values

869 when the number of clusters k varies from 2 to 12. The mean silhouette width values (red
870 diamond shaped points) attained their maximum when the estimated cluster number was 5.
871 (C) 3D plot showing cluster distribution of embryonic $V1^R$ according to log mean ½Ad, CV
872 ½Ad and log ddr. Each cluster corresponds to a particular firing pattern as illustrated in D.
873 $V1^R$ that cannot sustain repetitive firing of APs (1 to 3 AP/pulse only, gray, Single spiking, SS),
874 $V1^R$ that can fire tonically (red, Repetitive spiking, RS), $V1^R$ with a firing pattern characterized
875 by a mix of APs and relatively short plateau potentials (dark purple, Mixed event short PP,
876 ME short PP), $V1^R$ with a firing pattern characterized by a mix of APs and relatively long
877 plateau potentials (light purple, Mixed event long PP, ME long PP) and $V1^R$ with evoked
878 plateau potentials only (blue, Plateau potential, PP). The arrow in C indicates 3 misclassified
879 $V1^R$ that could not sustain repetitive firing although they were assigned to the cluster of
880 repetitively firing $V1^R$ (see text).
881
882 **Figure 4. Developmental changes of embryonic $V1^R$ firing patterns from E11.5 to E16.5**
883 (A1) Graph showing how the input capacitance C_{in} of $V1^R$ changes with embryonic age. C_{in}
884 significantly increased between E12.5 or E13.5 and E14.5 (Kruskall-Wallis test $P < 0.0001$;
885 E12.5 versus E11.5 $P = 0.258$, E12.5 versus E13.5 $P = 0.904$, E12.5 versus E14.5 $P < 0.0001$,
886 E12.5 versus E15.5 $P < 0.0001$, E12.5 versus E16.5 $P < 0.0001$, E13.5 versus E14.5 $P < 0.0001$,
887 E13.5 versus E15.5 $P < 0.0001$, E13.5 versus E16.5 $P < 0.0001$; E11.5 n = 31; N = 27, E12.5 n =
888 267; N = 152, E13.5 n = 43; N = 40, E14.5 n = 61; N = 49, E15.5 n = 16; N = 4, E16.5 n = 30; N =
889 9). (A2) Graph showing how the input resistance R_{in} of $V1^R$ changes with embryonic age. R_{in}
890 significantly decreased between E12.5 or E14.5 and E15.5 (Kruskall-Wallis test $P < 0.0001$;
891 E12.5 versus E11.5 $P > 0.999$, E12.5 versus E13.5 $P = 0.724$, E12.5 versus E14.5 $P > 0.999$,
892 E12.5 versus E15.5 $P = 0.0004$, E12.5 versus E16.5 $P = 0.0005$, E14.5 versus E15.5 $P = 0.0019$,

893 E14.5 versus E16.5 $P < 0.0058$; E11.5 n = 31, E12.5 n = 261; N = 146, E13.5 n = 43; N = 40,
894 E14.5 n = 60; N = 48, E15.5 n = 16; N = 4, E16.5 n = 30; N = 9). (A3) Graph showing how the
895 threshold of regenerative events (APs and plateau potentials) of $V1^R$ changes with
896 embryonic age. The average threshold became significantly more hyperpolarized after E12.5
897 (Kruskall-Wallis test $P < 0.0001$; E12.5 versus E11.5 $P = 0.676$, E12.5 versus E13.5 $P = 0.0039$,
898 E12.5 versus E14.5 $P < 0.0001$, E12.5 versus E15.5 $P < 0.0001$, E12.5 versus E16.5 $P < 0.0001$,
899 E13.5 versus E14.5 $P > 0.999$, E13.5 versus E15.5 $P = 0.1398$, E13.5 versus E16.5 $P = 0.0013$;
900 E14.5 versus E15.5 $P > 0.999$, E14.5 versus E16.5 $P = 0.0634$, E15.5 versus E16.5 $P > 0.999$;
901 E11.5 n = 20; N = 16, E12.5 n = 162; N = 139, E13.5 n = 31; N = 28, E14.5 n = 30; N = 26, E15.5
902 n = 16; N = 4, E16.5 n = 30; N = 9). Yellow and purple bars below the graphs indicate the two
903 important phases of the functional development of spinal cord networks. The first one is
904 characterized by synchronized neuronal activity (SNA) and the second one is characterized
905 by the emergence of a locomotor-like activity (see text). Note that changes in C_{in} and
906 R_{in} occurred at the end of the first developmental phase. (*$P < 0.05$, ** $P < 0.01$, *** $P <$
907 0.001; control, E12.5). The intrinsic activation properties were analyzed using 2 s
908 suprathreshold depolarizing current steps. (B) Representative traces of voltage responses
909 showing Single Spiking (SS) $V1^R$ (gray), Repetitive Spiking (RS) $V1^R$ (red), ME $V1^R$ (purple) and
910 Plateau Potential (PP) $V1^R$ (blue) at E11.5 (B1), E13.5 (B2), E14.5 (B3) E15.5 (B4) and E16.5
911 (B5). (C) Bar graph showing how the proportions of the different firing patterns change from
912 E11.5 to E16.5 (E11.5 n = 22; N = 18, E12.5 n = 163; N = 140, E13.5 n = 32; N = 29, E14.5 n =
913 57; N = 45, E15.5 n = 15; N = 4, E16.5 n = 28; N = 9). Yellow and purple bars below the graphs
914 indicate the first and the second phase of functional embryonic spinal cord networks. The
915 proportions of the different firing patterns significantly changed between E11.5 to E12.5
916 (Fisher's exact test, $P = 0.0052$) with a significant increase in the proportion of RS $V1^R$

917 (Fisher's exact test, *P* = 0.0336) and a significant decrease in the proportion of ME $V1^R$
918 (Fisher's exact test, *P* = 0.01071) at E12.5. Only two firing patterns (SS and RS) were observed
919 after E13.5 and most embryonic $V1^R$ lost their ability to sustain tonic firing after E13.5.
920 However, at E16.5 the proportion of RS $V1^R$ significantly increased at the expense of SS $V1^R$
921 when compared to E14.5 (Fisher's exact test, *P* = 0.0112), indicating that embryonic $V1^R$
922 began to recover the ability to sustain tonic firing after E15.5.
923
924 **Figure 5. Activated caspase-3 is not observed in embryonic $V1^R$ at E14.5**
925 Representative confocal image of the ventral part of an isolated lumbar spinal cord of E14.5
926 GAD67-eGFP mouse embryo showing immunostainings using antibodies against eGFP (A),
927 FoxD3 (B) and activated Caspase 3 (aCaspace 3) (C). (D) Superimposition of the three
928 stainings shows that embryonic $V1^R$ (eGFP+ and FoxD3+) were not aCaspase 3
929 immunoreactive. (A1, B1, C1 and D1). Enlarged images from A, B and C showing that
930 aCaspase 3 staining is localized in areas where eGFP and Foxd3 staining were absent. (A2, B2,
931 C2 and D2) Enlarged images from A, B and C showing that aCaspase 3 staining is absent in
932 the area where $V1^R$ (eGFP+ and FoxD3+) are located. aCaspase 3 staining that did not co-
933 localize with GAD67eGFP likely indicates MN developmental cell death.
934
935 **Figure 6. 600 μM 4-AP changed the firing pattern of single spiking embryonic $V1^R$ recorded**
936 **at E14.5**
937 The firing pattern of embryonic $V1^R$ was evoked by 2 s suprathreshold depolarizing current
938 steps. (A) Representative traces showing the effect of 4-AP application (600 μM) on the
939 firing pattern of single spiking (SS) $V1^R$ recorded at E14.5. Note that the applications of 600
940 μM 4-AP evoked either a plateau potential (A1) or repetitive spiking (A2), both fully blocked

941 by TTX. (B) Bar plots showing the proportions of the different firing patterns observed in the
942 presence of 600 µM 4-AP versus control recorded in SS $V1^R$ at E14.5 (n = 14; N = 14). Single
943 Spiking (SS) $V1^R$ (gray), Repetitive Spiking (RS) $V1^R$ (red), Mixed Events (ME) $V1^R$ (purple),
944 Plateau Potential (PP) $V1^R$ (blue).
945
946 **Figure 7. Embryonic $V1^R$ firing patterns predicted by computational modeling**
947 (A) Firing patterns of 27 recorded cells, in which both G_{Nap} and G_{Kdr} were measured. Gray:
948 SS, red: RS, blue: PP. The three purple points located at the boundary between the RS and PP
949 regions correspond to mixed events (ME) where plateau potentials alternate with spiking
950 episodes. Note that no cell exhibited low values of both G_{Nap} and G_{Kdr} (lower left), or large
951 values of both conductances (upper right). (B) Bifurcation diagram of the deterministic
952 model when G_{Kdr} is kept fixed to 2.5 nS or 10 nS while G_{Nap} is varied between 0 and 2.5 nS.
953 G_{in} = 1 nS and I = 20 pA. For G_{Kdr} = 10 nS (i.e., in the top experimental range), the red
954 curves indicate the maximal and minimal voltages achieved on the stable limit cycle
955 associated with repetitive firing (solid lines) and on the unstable limit cycle (dashed lines).
956 The fixed point of the model is indicated by a gray solid line when it corresponds to the
957 stable quiescent state, a gray dashed line when it is unstable and a solid blue line when it
958 corresponds to a stable plateau potential. The two HB corresponding to the change of
959 stability of the quiescence state (HB_1, G_{Nap}= 0.81 nS) and of the voltage plateau (HB_2, G_{Nap}=
960 2.13 nS) are indicated, as well as the two SN bifurcations of limit cycles associated with the
961 onset (SN_1, $G_{Nap} = 0.65$ nS) and offset (SN_2, G_{Nap}= 2.42 nS) of repetitive spiking as G_{Nap} is
962 increased. For G_{Kdr} = 2.5 nS, the model does not display repetitive firing; it possesses a
963 unique fixed point, which is always stable (blue-gray curve). The transition from quiescence
964 to plateau is gradual with no intervening bifurcation. Representative voltage traces of the

965 three different activity patterns are shown: single spiking in response to a 2 s current pulse
966 (gray, G_{Nap} = 0.2 nS, G_{Kdr} = 10 nS), repetitive spiking (red, G_{Nap} = 1.2 nS, G_{Kdr} = 10 nS) and
967 plateau potential (blue, G_{Nap} = 1.2 nS, G_{Kdr} = 2.5 nS). Note that the plateau never outlasts
968 the current pulse. (C) Bifurcation diagram when G_{Nap} is kept fixed at 1.2 nS and G_{Kdr} is
969 varied between 0 and 25 nS (I = 20 pA). Same conventions as in B. Plateau potential is stable
970 until the subcritical Hopf bifurcation HB_2 (G_{Kdr} = 6.34 nS) is reached, repetitive firing can be
971 observed between SN_2 (G_{Kdr} = 5.93 nS) and SN_1 (G_{Kdr} = 22.65 nS). The quiescent state is
972 stable from point HB_1 (G_{Kdr} = 17.59 nS) onward. (D) Two-parameters bifurcation diagram of
973 the model in the G_{Nap} - G_{Kdr} plane (I = 20 pA). The black merged curves indicate the
974 bifurcations HB_1 and HB_2. The red curves indicate the SN bifurcations of limit cycles SN_1 and
975 SN_2. The shaded area indicates the region where repetitive firing can occur. The oblique lines
976 through the points labeled 1, 2 and 3, the same as in B, correspond to three different values
977 of the ratio G_{Nap}/G_{Kdr} : 0.02 (gray), 0.12 (red) and 0.48 (blue). Voltage traces on the right
978 display the response to a 2 s current pulse when channel noise is taken into account for the
979 three regimes: quiescence (top, gray trace and dot in the diagram), repetitive firing (middle,
980 red) and plateau potential (bottom, blue). They correspond to the three deterministic
981 voltage traces shown in B. Note that the one-parameter bifurcation diagrams shown in B
982 correspond to horizontal lines through points 1 and 2 (G_{Kdr} = 10 nS) and through point 3
983 (G_{Kdr} = 2.5 nS), respectively. The bifurcation diagram in C corresponds to a vertical line
984 through point 2 and 3 (G_{Nap} = 1.2 nS). (E) Cumulative distribution function of the ratio
985 G_{Nap}/G_{Kdr} for the four clusters in A, showing the sequencing SS (gray) → RS (red) → ME
986 (purple, 3 cells only) → PP (blue) predicted by the two-parameters bifurcation diagram in D.
987 The wide PP range, as compared to SS and RS, merely comes from the fact that G_{Kdr} is small
988 for cells in this cluster. The three colored points indicate the slopes of the oblique lines

989 displayed in D (0.02, 0.12 and 0.48, respectively). (F) The data points in A are superimposed
990 on the two-parameters bifurcation diagram shown in D, demonstrating a good agreement
991 between our basic model and experimental data (the same color code as in A for the
992 different clusters). The bifurcation diagram is simplified compared to A, only the region
993 where repetitive spiking is possible (i.e. between the lines SN_1 and SN_2 in A) being displayed
994 (shaded area). Notice that 3 ME cells (purple dots) are located close to the transition
995 between the RS and PP regions. The four arrows indicate the presumable evolution of G_{Nap}
996 and G_{Kdr} for SS, RS, ME and PP cells between E12.5 and E14.5-15.5. G_{Nap} eventually
997 decreases while G_{Kdr} keeps on increasing. (G) Distribution of a sample of cells in the G_{Kdr} -
998 G_{Kdr} plane at E14.5. All the cells are located well within the SS region far from bifurcation
999 lines because of the decreased G_{Nap} compared to E12.5, the increased G_{Kdr}, and the shift of
1000 the RS region (shaded) due to capacitance increase (18 versus 13 pF).
1001
1002 **Figure 8. Effects of the slow inactivation of I_{Nap} on firing patterns predicted by**
1003 **computational modeling**
1004 (A) Examples of repetitive plateaus (left) and mixed events (right) recorded in $V1^R$ at E12.5
1005 during a 2 s current pulse. (B1) Current-voltage curve of the basic model (without slow
1006 inactivation of I_{Nap}, and without I_A or channel noise) for G_{Kdr} = 5 nS and for G_{Nap} = 1.65 nS
1007 (lower curve) and 2 nS (upper curve). Solid lines denote stable fixed points and dashed lines
1008 unstable ones. For G_{Nap} =1.65 nS, bistability between quiescence and plateau occurs
1009 between 1.39 and 10.48 pA. When G_{Nap} is increased to 2 nS, the bistability region ranges
1010 from -10.84 to 9.70 pA, thus extending into the negative current range. This implies that
1011 once a plateau has been elicited, the model will stay in that stable state and not return to
1012 the resting state, even though current injection is switched off (see insert). B1 Insert. Voltage

1013 response to a 2 s current pulse of 15 pA for G_{Nap} = 2 nS. The resting state (gray dot on the
1014 lower curve in B1 is destabilized at pulse onset and a plateau is elicited (blue dot on the
1015 upper curve in B1). At pulse offset, the plateau is maintained, even though the injected
1016 current is brought back to zero, and channel noise is not sufficient to go back to the resting
1017 state. (B2) Domain of bistability between quiescence and plateau (shaded) in the I-
1018 G_{Nap} plane for G_{Kdr}= 5 nS. It is delimited by the line SN_2 where a SN bifurcation of fixed
1019 points occurs and by the subcritical Hopf bifurcation line HB where the plateau becomes
1020 unstable. Bistability requires that G_{Nap} exceeds 1.35 nS, and the domain of bistability
1021 enlarges as G_{Nap} is increased further. The two horizontal lines correspond to the two cases
1022 shown in B1: G_{Nap} =1.65 nS and 2 nS. (C) Behavior of the model when slow inactivation is
1023 incorporated. The bifurcation diagram of the basic model (without slow inactivation) for I =
1024 10 pA and G_{Kdr} = 5 nS (same conventions as in Fig 7B) and the stable limit cycle (black solid
1025 curve) obtained when slow inactivation is added are superimposed. The limit cycle is
1026 comprised of four successive phases (see labels): 1) long plateau during which I_{Nap} slowly
1027 inactivates, 2) fast transition to the quiescent state, 3) repolarization episode during which
1028 I_{Nap} slowly deinactivates, 4) fast transition back to the plateau. Each plateau starts with a
1029 full-blown action potential followed by rapidly decaying spikelets. Note that the bifurcation
1030 HB is subcritical here (unstable limit cycle shown by dashed red curve), at variance with
1031 square wave bursting (supercritical bifurcation and stable limit cycle); this is a characteristic
1032 feature of pseudo-plateau bursting. Note also that the plateau extends beyond the
1033 bifurcation HB because it is only weakly unstable then. Responses to a 15 s current pulse are
1034 shown on the right side. Top left: voltage response, Top right: behavior of the "effective"
1035 conductance of I_{Nap} channel, i.e., the maximal conductance G_{Nap} multiplied by the slow
1036 inactivation variable s. Bottom left: voltage trace when channel noise is added to fast and

1037 slow gating variables, Bottom right: Voltage trace when G_{Nap} is increased by 50%. (D) Mixed
1038 events. The bifurcation diagram of the basic model for G_{Kdr} = 5 nS and I = 12 pA and the
1039 stable limit cycle obtained in the presence of slow inactivation (G_{Nap} = 2.5 nS) are
1040 superimposed. Here again, the limit cycle is comprised of four successive phases (see labels):
1041 1) slow inactivation of I_{Nap} that leads to the crossing of the bifurcation point HB_2 and then
1042 to the destabilization of the plateau potential, 2) fast transition to the spiking regime, 3)
1043 repetitive spiking during which I_{Nap} slowly de-inactivates, which leads to the crossing of the
1044 bifurcation point SN_2 and terminates the spiking episode, 4) fast transition back to the stable
1045 plateau potential. Response to a 15 s current pulse of 12 pA is shown on the right in the
1046 absence of any channel noise. Top: Voltage trace (same labels as in the bifurcation diagram
1047 on the left), Bottom: Variations of the "effective" conductance $G_{Nap}s$ (same labels as in the
1048 voltage trace). Note that de-inactivation sufficient to trigger a new plateau occurs over a
1049 series of successive spikes, hence the small oscillations are visible on the trace. Note also
1050 that in C and D the first plateau lasts longer than the following ones, as in
1051 electrophysiological recordings of embryonic $V1^R$ cells displaying repetitive plateaus. This
1052 form of adaptation is caused by the slow inactivation of the persistent sodium current.
1053

1054 ## References

1055 1. O'Donovan MJ. The origin of spontaneous activity in developing networks of the
1056 vertebrate nervous system. Curr Opin Neurobiol. 1999;9(1):94-104. PubMed PMID:
1057 10072366.
1058 2. Saint-Amant L. Development of motor rhythms in zebrafish embryos. Progress in
1059 brain research. 2010;187:47-61. doi: 10.1016/B978-0-444-53613-6.00004-6. PubMed PMID:
1060 21111200.
1061 3. Blankenship AG, Feller MB. Mechanisms underlying spontaneous patterned activity
1062 in developing neural circuits. Nature reviews Neuroscience. 2010;11(1):18-29. doi:
1063 10.1038/nrn2759. PubMed PMID: 19953103; PubMed Central PMCID: PMC2902252.
1064 4. Myers CP, Lewcock JW, Hanson MG, Gosgnach S, Aimone JB, Gage FH, et al.
1065 Cholinergic input is required during embryonic development to mediate proper assembly of
1066 spinal locomotor circuits. Neuron. 2005;46(1):37-49. Epub 2005/04/12. doi: S0896-
1067 6273(05)00165-0 [pii]
1068 10.1016/j.neuron.2005.02.022. PubMed PMID: 15820692.
1069 5. Milner LD, Landmesser LT. Cholinergic and GABAergic inputs drive patterned
1070 spontaneous motoneuron activity before target contact. J Neurosci. 1999;19(8):3007-22.
1071 PubMed PMID: 10191318.
1072 6. Hanson MG, Landmesser LT. Characterization of the circuits that generate
1073 spontaneous episodes of activity in the early embryonic mouse spinal cord. J Neurosci.
1074 2003;23(2):587-600. PubMed PMID: 12533619.
1075 7. Momose-Sato Y, Sato K. Large-scale synchronized activity in the embryonic
1076 brainstem and spinal cord. Frontiers in cellular neuroscience. 2013;7:36. doi:
1077 10.3389/fncel.2013.00036. PubMed PMID: 23596392; PubMed Central PMCID:
1078 PMC3625830.
1079 8. Khazipov R, Luhmann HJ. Early patterns of electrical activity in the developing
1080 cerebral cortex of humans and rodents. Trends in neurosciences. 2006;29(7):414-8. doi:
1081 10.1016/j.tins.2006.05.007. PubMed PMID: 16713634.
1082 9. Allain AE, Le Corronc H, Delpy A, Cazenave W, Meyrand P, Legendre P, et al.
1083 Maturation of the GABAergic transmission in normal and pathologic motoneurons. Neural
1084 plasticity. 2011;2011:905624. doi: 10.1155/2011/905624. PubMed PMID: 21785735;
1085 PubMed Central PMCID: PMC3140191.
1086 10. Branchereau P, Chapron J, Meyrand P. Descending 5-hydroxytryptamine raphe inputs
1087 repress the expression of serotonergic neurons and slow the maturation of inhibitory systems

1088 in mouse embryonic spinal cord. J Neurosci. 2002;22(7):2598-606. doi: 20026199. PubMed
1089 PMID: 11923425.
1090 11. Yvert B, Branchereau P, Meyrand P. Multiple spontaneous rhythmic activity patterns
1091 generated by the embryonic mouse spinal cord occur within a specific developmental time
1092 window. Journal of neurophysiology. 2004;91(5):2101-9. doi: 10.1152/jn.01095.2003.
1093 PubMed PMID: 14724265.
1094 12. Czarnecki A, Le Corronc H, Rigato C, Le Bras B, Couraud F, Scain AL, et al.
1095 Acetylcholine controls GABA-, glutamate-, and glycine-dependent giant depolarizing
1096 potentials that govern spontaneous motoneuron activity at the onset of synaptogenesis in the
1097 mouse embryonic spinal cord. J Neurosci. 2014;34(18):6389-404. doi:
1098 10.1523/JNEUROSCI.2664-13.2014. PubMed PMID: 24790209.
1099 13. Pun S, Sigrist M, Santos AF, Ruegg MA, Sanes JR, Jessell TM, et al. An intrinsic
1100 distinction in neuromuscular junction assembly and maintenance in different skeletal muscles.
1101 Neuron. 2002;34(3):357-70. doi: 10.1016/s0896-6273(02)00670-0. PubMed PMID:
1102 11988168.
1103 14. Angelim M, Maia L, Mouffle C, Ginhoux F, Low D, Amancio-Dos-Santos A, et al.
1104 Embryonic macrophages and microglia ablation alter the development of dorsal root ganglion
1105 sensory neurons in mouse embryos. Glia. 2018;66(11):2470-86. doi: 10.1002/glia.23499.
1106 PubMed PMID: 30252950.
1107 15. Marmigere F, Ernfors P. Specification and connectivity of neuronal subtypes in the
1108 sensory lineage. Nature reviews Neuroscience. 2007;8(2):114-27. doi: 10.1038/nrn2057.
1109 PubMed PMID: 17237804.
1110 16. Ozaki S, Snider WD. Initial trajectories of sensory axons toward laminar targets in the
1111 developing mouse spinal cord. The Journal of comparative neurology. 1997;380(2):215-29.
1112 PubMed PMID: 9100133.
1113 17. Ballion B, Branchereau P, Chapron J, Viala D. Ontogeny of descending serotonergic
1114 innervation and evidence for intraspinal 5-HT neurons in the mouse spinal cord. Brain
1115 research Developmental brain research. 2002;137(1):81-8. doi: 10.1016/s0165-
1116 3806(02)00414-5. PubMed PMID: 12128257.
1117 18. Moody WJ, Bosma MM. Ion channel development, spontaneous activity, and activity-
1118 dependent development in nerve and muscle cells. Physiological reviews. 2005;85(3):883-941.
1119 doi: 10.1152/physrev.00017.2004. PubMed PMID: 15987798.
1120 19. Spitzer NC. Electrical activity in early neuronal development. Nature.
1121 2006;444(7120):707-12. doi: 10.1038/nature05300. PubMed PMID: 17151658.

1122 20. Katz LC, Shatz CJ. Synaptic activity and the construction of cortical circuits. Science.
1123 1996;274(5290):1133-8. PubMed PMID: 8895456.
1124 21. Hanson MG, Milner LD, Landmesser LT. Spontaneous rhythmic activity in early
1125 chick spinal cord influences distinct motor axon pathfinding decisions. Brain Res Rev.
1126 2008;57(1):77-85. Epub 2007/10/09. doi: S0165-0173(07)00127-0 [pii]
1127 10.1016/j.brainresrev.2007.06.021. PubMed PMID: 17920131.
1128 22. Hanson MG, Landmesser LT. Normal patterns of spontaneous activity are required for
1129 correct motor axon guidance and the expression of specific guidance molecules. Neuron.
1130 2004;43(5):687-701. doi: 10.1016/j.neuron.2004.08.018. PubMed PMID: 15339650.
1131 23. Hanson MG, Landmesser LT. Increasing the frequency of spontaneous rhythmic
1132 activity disrupts pool-specific axon fasciculation and pathfinding of embryonic spinal
1133 motoneurons. J Neurosci. 2006;26(49):12769-80. doi: 10.1523/JNEUROSCI.4170-06.2006.
1134 PubMed PMID: 17151280.
1135 24. Benito-Gonzalez A, Alvarez FJ. Renshaw cells and Ia inhibitory interneurons are
1136 generated at different times from p1 progenitors and differentiate shortly after exiting the cell
1137 cycle. J Neurosci. 2012;32(4):1156-70. doi: 10.1523/JNEUROSCI.3630-12.2012. PubMed
1138 PMID: 22279202; PubMed Central PMCID: PMC3276112.
1139 25. Boeri J, Le Corronc H, Lejeune FX, Le Bras B, Mouffle C, Angelim M, et al.
1140 Persistent Sodium Current Drives Excitability of Immature Renshaw Cells in Early
1141 Embryonic Spinal Networks. J Neurosci. 2018;38(35):7667-82. doi:
1142 10.1523/JNEUROSCI.3203-17.2018. PubMed PMID: 30012693.
1143 26. Perry S, Gezelius H, Larhammar M, Hilscher MM, Lamotte d'Incamps B, Leao KE, et
1144 al. Firing properties of Renshaw cells defined by Chrna2 are modulated by hyperpolarizing
1145 and small conductance ion currents Ih and ISK. The European journal of neuroscience.
1146 2015;41(7):889-900. doi: 10.1111/ejn.12852. PubMed PMID: 25712471.
1147 27. Bikoff JB, Gabitto MI, Rivard AF, Drobac E, Machado TA, Miri A, et al. Spinal
1148 Inhibitory Interneuron Diversity Delineates Variant Motor Microcircuits. Cell.
1149 2016;165(1):207-19. doi: 10.1016/j.cell.2016.01.027. PubMed PMID: 26949184; PubMed
1150 Central PMCID: PMC4808435.
1151 28. Delpy A, Allain AE, Meyrand P, Branchereau P. NKCC1 cotransporter inactivation
1152 underlies embryonic development of chloride-mediated inhibition in mouse spinal
1153 motoneuron. J Physiol. 2008;586(4):1059-75. doi: 10.1113/jphysiol.2007.146993. PubMed
1154 PMID: 18096599; PubMed Central PMCID: PMC2375629.

1155 29. Crill WE. Persistent sodium current in mammalian central neurons. Annual review of
1156 physiology. 1996;58:349-62. doi: 10.1146/annurev.ph.58.030196.002025. PubMed PMID:
1157 8815799.
1158 30. Sillar KT, Simmers AJ, Wedderburn JF. The post-embryonic development of cell
1159 properties and synaptic drive underlying locomotor rhythm generation in Xenopus larvae.
1160 Proceedings Biological sciences. 1992;249(1324):65-70. doi: 10.1098/rspb.1992.0084.
1161 PubMed PMID: 1359549.
1162 31. Gao BX, Ziskind-Conhaim L. Development of ionic currents underlying changes in
1163 action potential waveforms in rat spinal motoneurons. Journal of neurophysiology.
1164 1998;80(6):3047-61. PubMed PMID: 9862905.
1165 32. Gao H, Lu Y. Early development of intrinsic and synaptic properties of chicken
1166 nucleus laminaris neurons. Neuroscience. 2008;153(1):131-43. doi:
1167 10.1016/j.neuroscience.2008.01.059. PubMed PMID: 18355968.
1168 33. McKay BE, Turner RW. Physiological and morphological development of the rat
1169 cerebellar Purkinje cell. J Physiol. 2005;567(Pt 3):829-50. doi: 10.1113/jphysiol.2005.089383.
1170 PubMed PMID: 16002452; PubMed Central PMCID: PMC1474219.
1171 34. Liu X, Pfaff DW, Calderon DP, Tabansky I, Wang X, Wang Y, et al. Development of
1172 Electrophysiological Properties of Nucleus Gigantocellularis Neurons Correlated with
1173 Increased CNS Arousal. Developmental neuroscience. 2016;38(4):295-310. doi:
1174 10.1159/000449035. PubMed PMID: 27788521; PubMed Central PMCID: PMC5127753.
1175 35. Pineda R, Ribera A. Evolution of the Action Potential. In: Kaas JH, editor. Evolution
1176 of Nervous Systems. 1: Elsevier Ltd; 2010. p. 211-38.
1177 36. Coetzee WA, Amarillo Y, Chiu J, Chow A, Lau D, McCormack T, et al. Molecular
1178 diversity of K+ channels. Annals of the New York Academy of Sciences. 1999;868:233-85.
1179 doi: 10.1111/j.1749-6632.1999.tb11293.x. PubMed PMID: 10414301.
1180 37. O'Leary T, Williams AH, Caplan JS, Marder E. Correlations in ion channel expression
1181 emerge from homeostatic tuning rules. Proceedings of the National Academy of Sciences of
1182 the United States of America. 2013;110(28):E2645-54. Epub 2013/06/27. doi:
1183 10.1073/pnas.1309966110. PubMed PMID: 23798391; PubMed Central PMCID:
1184 PMCPMC3710808.
1185 38. Taylor AL, Goaillard JM, Marder E. How multiple conductances determine
1186 electrophysiological properties in a multicompartment model. J Neurosci. 2009;29(17):5573-
1187 86. Epub 2009/05/01. doi: 10.1523/jneurosci.4438-08.2009. PubMed PMID: 19403824;
1188 PubMed Central PMCID: PMCPMC2821064.

1189 39. Alonso LM, Marder E. Visualization of currents in neural models with similar
1190 behavior and different conductance densities. eLife. 2019;8. Epub 2019/02/01. doi:
1191 10.7554/eLife.42722. PubMed PMID: 30702427; PubMed Central PMCID:
1192 PMCPMC6395073.
1193 40. Sigworth FJ, Sine SM. Data transformations for improved display and fitting of
1194 single-channel dwell time histograms. Biophysical journal. 1987;52(6):1047-54. doi:
1195 10.1016/S0006-3495(87)83298-8. PubMed PMID: 2447968; PubMed Central PMCID:
1196 PMC1330104.
1197 41. Ramoa AS, McCormick DA. Developmental changes in electrophysiological
1198 properties of LGNd neurons during reorganization of retinogeniculate connections. J Neurosci.
1199 1994;14(4):2089-97. PubMed PMID: 8158259; PubMed Central PMCID: PMC6577110.
1200 42. Belleau ML, Warren RA. Postnatal development of electrophysiological properties of
1201 nucleus accumbens neurons. Journal of neurophysiology. 2000;84(5):2204-16. doi:
1202 10.1152/jn.2000.84.5.2204. PubMed PMID: 11067966.
1203 43. Picken Bahrey HL, Moody WJ. Early development of voltage-gated ion currents and
1204 firing properties in neurons of the mouse cerebral cortex. Journal of neurophysiology.
1205 2003;89(4):1761-73. doi: 10.1152/jn.00972.2002. PubMed PMID: 12611962.
1206 44. Tong H, McDearmid JR. Pacemaker and plateau potentials shape output of a
1207 developing locomotor network. Current biology : CB. 2012;22(24):2285-93. doi:
1208 10.1016/j.cub.2012.10.025. PubMed PMID: 23142042; PubMed Central PMCID:
1209 PMC3525839.
1210 45. Alvarez FJ, Benito-Gonzalez A, Siembab VC. Principles of interneuron development
1211 learned from Renshaw cells and the motoneuron recurrent inhibitory circuit. Annals of the
1212 New York Academy of Sciences. 2013;1279:22-31. doi: 10.1111/nyas.12084. PubMed PMID:
1213 23530999; PubMed Central PMCID: PMC3870136.
1214 46. Allain AE, Segu L, Meyrand P, Branchereau P. Serotonin controls the maturation of
1215 the GABA phenotype in the ventral spinal cord via 5-HT1b receptors. Annals of the New
1216 York Academy of Sciences. 2010;1198:208-19. doi: 10.1111/j.1749-6632.2010.05433.x.
1217 PubMed PMID: 20536936.
1218 47. Branchereau P, Morin D, Bonnot A, Ballion B, Chapron J, Viala D. Development of
1219 lumbar rhythmic networks: from embryonic to neonate locomotor-like patterns in the mouse.
1220 Brain research bulletin. 2000;53(5):711-8. doi: 10.1016/s0361-9230(00)00403-2. PubMed
1221 PMID: 11165805.

48. Spitzer NC, Vincent A, Lautermilch NJ. Differentiation of electrical excitability in motoneurons. Brain research bulletin. 2000;53(5):547-52. PubMed PMID: 11165790.

49. Prasad T, Wang X, Gray PA, Weiner JA. A differential developmental pattern of spinal interneuron apoptosis during synaptogenesis: insights from genetic analyses of the protocadherin-gamma gene cluster. Development. 2008;135(24):4153-64. doi: 10.1242/dev.026807. PubMed PMID: 19029045; PubMed Central PMCID: PMC2755264.

50. Taddese A, Bean BP. Subthreshold sodium current from rapidly inactivating sodium channels drives spontaneous firing of tuberomammillary neurons. Neuron. 2002;33(4):587-600. doi: 10.1016/s0896-6273(02)00574-3. PubMed PMID: 11856532.

51. Kuo JJ, Lee RH, Zhang L, Heckman CJ. Essential role of the persistent sodium current in spike initiation during slowly rising inputs in mouse spinal neurones. J Physiol. 2006;574(Pt 3):819-34. doi: 10.1113/jphysiol.2006.107094. PubMed PMID: 16728453; PubMed Central PMCID: PMC1817738.

52. Teka W, Tsaneva-Atanasova K, Bertram R, Tabak J. From plateau to pseudo-plateau bursting: making the transition. Bulletin of mathematical biology. 2011;73(6):1292-311. doi: 10.1007/s11538-010-9559-7. PubMed PMID: 20658200; PubMed Central PMCID: PMC3152987.

53. Bertram R, Butte MJ, Kiemel T, Sherman A. Topological and phenomenological classification of bursting oscillations. Bulletin of mathematical biology. 1995;57(3):413-39. doi: 10.1007/BF02460633. PubMed PMID: 7728115.

54. Izhikevich EM. Neural excitability, spiking and bursting. Int J Bifurcation Chaos. 2000;10(06):1171-266.

55. Borisyuk A, Rinzel J. Understanding neuronal dynamics by geometrical dissection of minimal models. In: Chow C, Gutkin B, Hansel D, Meunier C, Dalibard J, editors. Models and Methods in Neurophysics. Proc Les Houches Summer School 2003, (Session LXXX): Elsevier; 2005. p. 19-72.

56. Rinzel J. Bursting oscillations in an excitable membrane model. In: Sleeman B, Jarvis R, editors. Ordinary and Partial Differential Equations Lecture Notes in Mathematics. 1151. Berlin, Heidelberg: Springer; 1985. p. 304–16.

57. Stern JV, Osinga HM, LeBeau A, Sherman A. Resetting behavior in a model of bursting in secretory pituitary cells: distinguishing plateaus from pseudo-plateaus. Bulletin of mathematical biology. 2008;70(1):68-88. doi: 10.1007/s11538-007-9241-x. PubMed PMID: 17703340.

1255 58. Osinga HM, Tsaneva-Atanasova KT. Dynamics of plateau bursting depending on the
1256 location of its equilibrium. Journal of neuroendocrinology. 2010;22(12):1301-14. doi:
1257 10.1111/j.1365-2826.2010.02083.x. PubMed PMID: 20955345.
1258 59. Osinga HM, Sherman A, Tsaneva-Atanasova K. Cross-Currents between Biology and
1259 Mathematics: The Codimension of Pseudo-Plateau Bursting. Discrete and continuous
1260 dynamical systems Series A. 2012;32(8):2853-77. doi: 10.3934/dcds.2012.32.2853. PubMed
1261 PMID: 22984340; PubMed Central PMCID: PMC3439852.
1262 60. Izhikevich EM. Subcritical Elliptic Bursting of Bautin Type. SIAM Journal on
1263 Applied Mathematics. 2000;60(2):503-35. doi: https://doi.org/10.1137/S003613999833263X.
1264 61. Su J, Rubin J, Terman D. Effects of noise on elliptic bursters. Nonlinearity.
1265 2004;17(1):133-57. doi: https://doi.org/10.1088/0951-7715/17/1/009.
1266 62. Stam FJ, Hendricks TJ, Zhang J, Geiman EJ, Francius C, Labosky PA, et al. Renshaw
1267 cell interneuron specialization is controlled by a temporally restricted transcription factor
1268 program. Development. 2012;139(1):179-90. doi: 10.1242/dev.071134. PubMed PMID:
1269 22115757; PubMed Central PMCID: PMC3231776.
1270 63. Eccles JC, Fatt P, Landgren S. The inhibitory pathway to motoneurones. Progress in
1271 neurobiology. 1956;(2):72-82. PubMed PMID: 13441782.
1272 64. Vinay L, Brocard F, Clarac F. Differential maturation of motoneurons innervating
1273 ankle flexor and extensor muscles in the neonatal rat. The European journal of neuroscience.
1274 2000;12(12):4562-6. doi: 10.1046/j.0953-816x.2000.01321.x. PubMed PMID: 11122369.
1275 65. Durand J, Filipchuk A, Pambo-Pambo A, Amendola J, Borisovna Kulagina I,
1276 Gueritaud JP. Developing electrical properties of postnatal mouse lumbar motoneurons.
1277 Frontiers in cellular neuroscience. 2015;9:349. doi: 10.3389/fncel.2015.00349. PubMed
1278 PMID: 26388736; PubMed Central PMCID: PMC4557103.
1279 66. Marcotti W, Johnson SL, Holley MC, Kros CJ. Developmental changes in the
1280 expression of potassium currents of embryonic, neonatal and mature mouse inner hair cells. J
1281 Physiol. 2003;548(Pt 2):383-400. doi: 10.1113/jphysiol.2002.034801. PubMed PMID:
1282 12588897; PubMed Central PMCID: PMC2342842.
1283 67. Marcotti W, Johnson SL, Rusch A, Kros CJ. Sodium and calcium currents shape
1284 action potentials in immature mouse inner hair cells. J Physiol. 2003;552(Pt 3):743-61. doi:
1285 10.1113/jphysiol.2003.043612. PubMed PMID: 12937295; PubMed Central PMCID:
1286 PMC2343463.
1287 68. Sontheimer H, Trotter J, Schachner M, Kettenmann H. Channel expression correlates
1288 with differentiation stage during the development of oligodendrocytes from their precursor

1289 cells in culture. Neuron. 1989;2(2):1135-45. doi: 10.1016/0896-6273(89)90180-3. PubMed
1290 PMID: 2560386.
1291 69. Allain AE, Bairi A, Meyrand P, Branchereau P. Ontogenic changes of the GABAergic
1292 system in the embryonic mouse spinal cord. Brain research. 2004;1000(1-2):134-47. doi:
1293 10.1016/j.brainres.2003.11.071. PubMed PMID: 15053961.
1294 70. Sapir T, Geiman EJ, Wang Z, Velasquez T, Mitsui S, Yoshihara Y, et al. Pax6 and
1295 engrailed 1 regulate two distinct aspects of renshaw cell development. J Neurosci.
1296 2004;24(5):1255-64. doi: 10.1523/JNEUROSCI.3187-03.2004. PubMed PMID: 14762144;
1297 PubMed Central PMCID: PMC2997484.
1298 71. Henley J, Poo MM. Guiding neuronal growth cones using Ca2+ signals. Trends in cell
1299 biology. 2004;14(6):320-30. doi: 10.1016/j.tcb.2004.04.006. PubMed PMID: 15183189;
1300 PubMed Central PMCID: PMC3115711.
1301 72. Tsaneva-Atanasova K, Osinga HM, Riess T, Sherman A. Full system bifurcation
1302 analysis of endocrine bursting models. Journal of theoretical biology. 2010;264(4):1133-46.
1303 doi: 10.1016/j.jtbi.2010.03.030. PubMed PMID: 20307553; PubMed Central PMCID:
1304 PMC3128456.
1305 73. Tagliavini A, Tabak J, Bertram R, Pedersen MG. Is bursting more effective than
1306 spiking in evoking pituitary hormone secretion? A spatiotemporal simulation study of calcium
1307 and granule dynamics. American journal of physiology Endocrinology and metabolism.
1308 2016;310(7):E515-25. doi: 10.1152/ajpendo.00500.2015. PubMed PMID: 26786781.
1309 74. Oster A, Faure P, Gutkin BS. Mechanisms for multiple activity modes of VTA
1310 dopamine neurons. Frontiers in computational neuroscience. 2015;9:95. doi:
1311 10.3389/fncom.2015.00095. PubMed PMID: 26283955; PubMed Central PMCID:
1312 PMC4516885.
1313 75. Chevalier M, Toporikova N, Simmers J, Thoby-Brisson M. Development of
1314 pacemaker properties and rhythmogenic mechanisms in the mouse embryonic respiratory
1315 network. eLife. 2016;5. doi: 10.7554/eLife.16125. PubMed PMID: 27434668; PubMed
1316 Central PMCID: PMC4990420.
1317 76. Kole MH, Stuart GJ. Signal processing in the axon initial segment. Neuron.
1318 2012;73(2):235-47. doi: 10.1016/j.neuron.2012.01.007. PubMed PMID: 22284179.
1319 77. Tamamaki N, Yanagawa Y, Tomioka R, Miyazaki J, Obata K, Kaneko T. Green
1320 fluorescent protein expression and colocalization with calretinin, parvalbumin, and
1321 somatostatin in the GAD67-GFP knock-in mouse. The Journal of comparative neurology.
1322 2003;467(1):60-79. doi: 10.1002/cne.10905. PubMed PMID: 14574680.

78. Scain AL, Le Corronc H, Allain AE, Muller E, Rigo JM, Meyrand P, et al. Glycine release from radial cells modulates the spontaneous activity and its propagation during early spinal cord development. J Neurosci. 2010;30(1):390-403. Epub 2010/01/08. doi: 30/1/390 [pii]
10.1523/JNEUROSCI.2115-09.2010. PubMed PMID: 20053920.
79. Huang H, Trussell LO. Control of presynaptic function by a persistent Na(+) current. Neuron. 2008;60(6):975-9. doi: 10.1016/j.neuron.2008.10.052. PubMed PMID: 19109905; PubMed Central PMCID: PMC2657474.
80. Rousseeuw PJ. Silhouettes - a Graphical Aid to the Interpretation and Validation of Cluster-Analysis. J Comput Appl Math. 1987;20:53-65. doi: Doi 10.1016/0377-0427(87)90125-7. PubMed PMID: WOS:A1987L111800005.
81. Ermentrout B. Simulating, Analyzing, and Animating Dynamical Systems: A Guide to XPPAUT for Researchers and Students. Philadelphia: Society for Industrial and Applied Mathematics; 2002.
82. Gillespie DT. A general method for numerically simulating the stochastic time evolution of coupled chemical reactions. Journal of Computational Physics. 1976;22(4):403-34. doi: https://doi.org/10.1016/0021-9991(76)90041-3.
83. Witelski T, Bowen M. Fast/slow Dynamical Systems. In: Methods of Mathematical Modelling: Springer, Cham; 2015.

Table 1

Parameter	Basic model	Model with slow inactivation of I_{Nap}
Passive parameters		
Input conductance G_{in}	1 nS	same
Input capacitance C_{in}	13 pF (E12.5, Figs. 7B, C, D and F and 8B to D) or 18 pF (E14.5, Fig. 7G)	13 pF
Resting potential V_r	-60 mV	same
Injected current I	20 pA (Fig. 7B to G)	10 pA (Fig. 8C) or 12 pA (Fig. 8D) variable in Fig. 8B
Transient sodium current I_{nat}		
Maximal conductance G_{Nat}	20 nS	same
Reversal potential E_{Na}	60 mV	
Activation exponent	3	
Mid-activation V_m	-26 mV	
Steepness of activation k_m	9.5 mV	
Activation time constant	1.5 ms	
Mid-inactivation V_h	-45 mV	
Steepness of inactivation K_h	-5 mV	
Inactivation time constant τ_m	Voltage-dependent (see Material and Methods)	
Persistent sodium current I_{Nap}		
Maximal conductance	variable (see text and figure captions)	same
Mid-activation voltage	-36 mV	same
Mid-inactivation V_s		-30 mV
Steepness of inactivation k_s		-5 mV
Inactivation time constant	Slow inactivation not included	2 s
Delayed rectifier potassium current I_{Kdr}		
Maximal conductance G_{Kdr}	variable (see text and figure captions)	same
Reversal potential E_K	-96 mV	
Activation exponent	3	
Mid-activation V_n	-20 mV	
Steepness of activation k_n	15 mV	
Activation time constant τ_m	10 ms	
Potassium A current I_A (when included in the basic model)		
Maximal conductance G_A	Equal to G_{Kdr}	never included
Mid-activation V_{mA}	-30 mV	
Steepness of activation k_{mA}	12 mV	
Activation time constant	Instantaneous activation	
Mid-inactivation V_{hA}	-70 mV	
Steepness of inactivation k_{hA}	-7 mV	
Inactivation time constant τ_{hA}	23 ms	

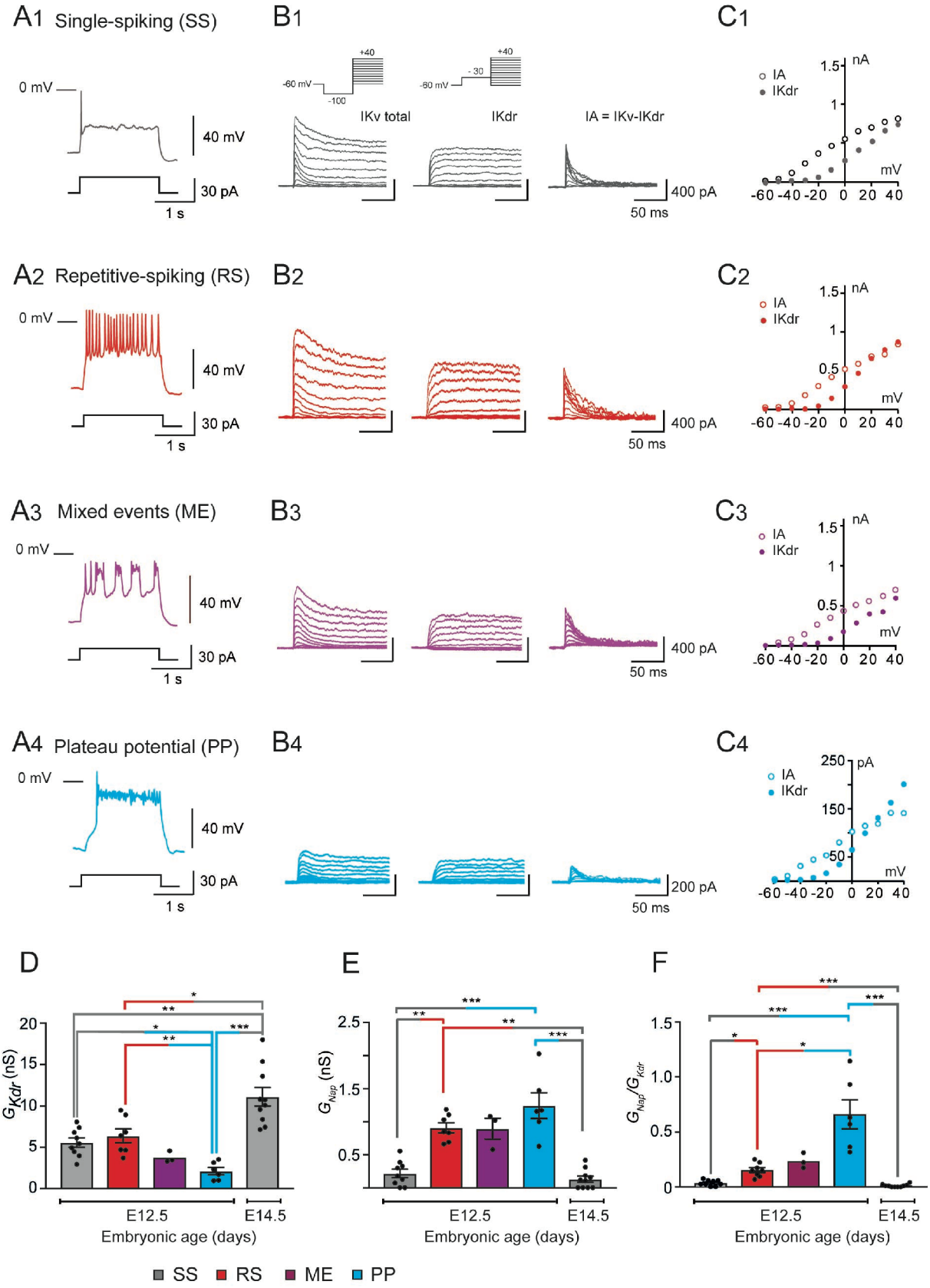
A1 Single-spiking (SS)
B1
C1
0 mV
40 mV
30 pA
1 s
+40
-60 mV
-100
-30
IKv total
IKdr
IA = IKv-IKdr
400 pA
50 ms
IA
IKdr
nA
mV
A2 Repetitive-spiking (RS)
B2
C2
A3 Mixed events (ME)
B3
C3
A4 Plateau potential (PP)
B4
C4
200 pA
pA
D
E
F
G_{Kdr} (nS)
G_{Nap} (nS)
G_{Nap}/G_{Kdr}
E12.5
E14.5
Embryonic age (days)
SS
RS
ME
PP

Fig 1

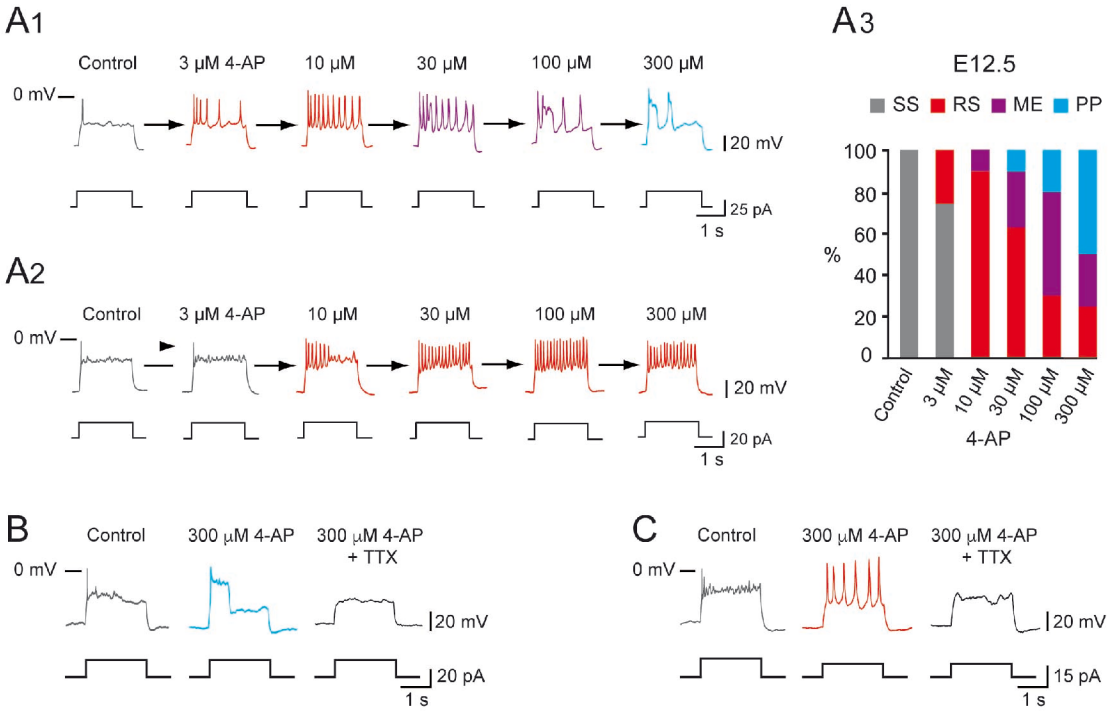
A1
Control
3 μM 4-AP
10 μM
30 μM
100 μM
300 μM
0 mV
20 mV
25 pA
1 s
A2
Control
3 μM 4-AP
10 μM
30 μM
100 μM
300 μM
0 mV
20 mV
20 pA
1 s
A3
E12.5
SS
RS
ME
PP
100
80
60
40
20
0
%
Control
3 μM
10 μM
30 μM
100 μM
300 μM
4-AP
B
Control
300 μM 4-AP
300 μM 4-AP
+ TTX
0 mV
20 mV
20 pA
1 s
C
Control
300 μM 4-AP
300 μM 4-AP
+ TTX
0 mV
20 mV
15 pA
1 s

Fig 2

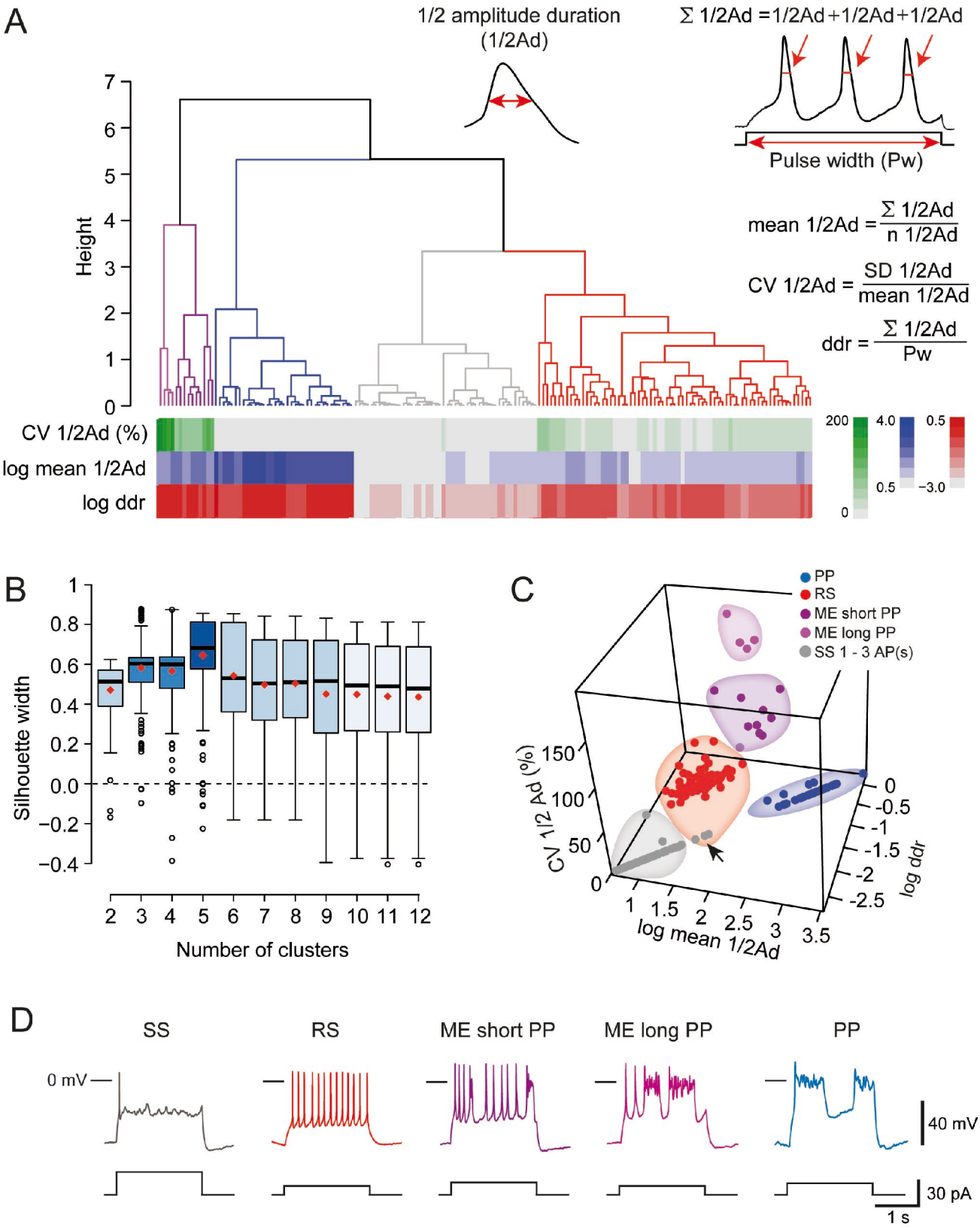
A
1/2 amplitude duration
(1/2Ad)
Σ 1/2Ad =1/2Ad+1/2Ad+1/2Ad
Pulse width (Pw)
mean 1/2Ad = Σ 1/2Ad / n 1/2Ad
CV 1/2Ad = SD 1/2Ad / mean 1/2Ad
ddr = Σ 1/2Ad / Pw
Height
CV 1/2Ad (%)
log mean 1/2Ad
log ddr
B
Silhouette width
Number of clusters
C
PP
RS
ME short PP
ME long PP
SS 1 - 3 AP(s)
CV 1/2 Ad (%)
log mean 1/2Ad
log ddr
D
SS
RS
ME short PP
ME long PP
PP
0 mV
40 mV
30 pA
1 s

Fig 3

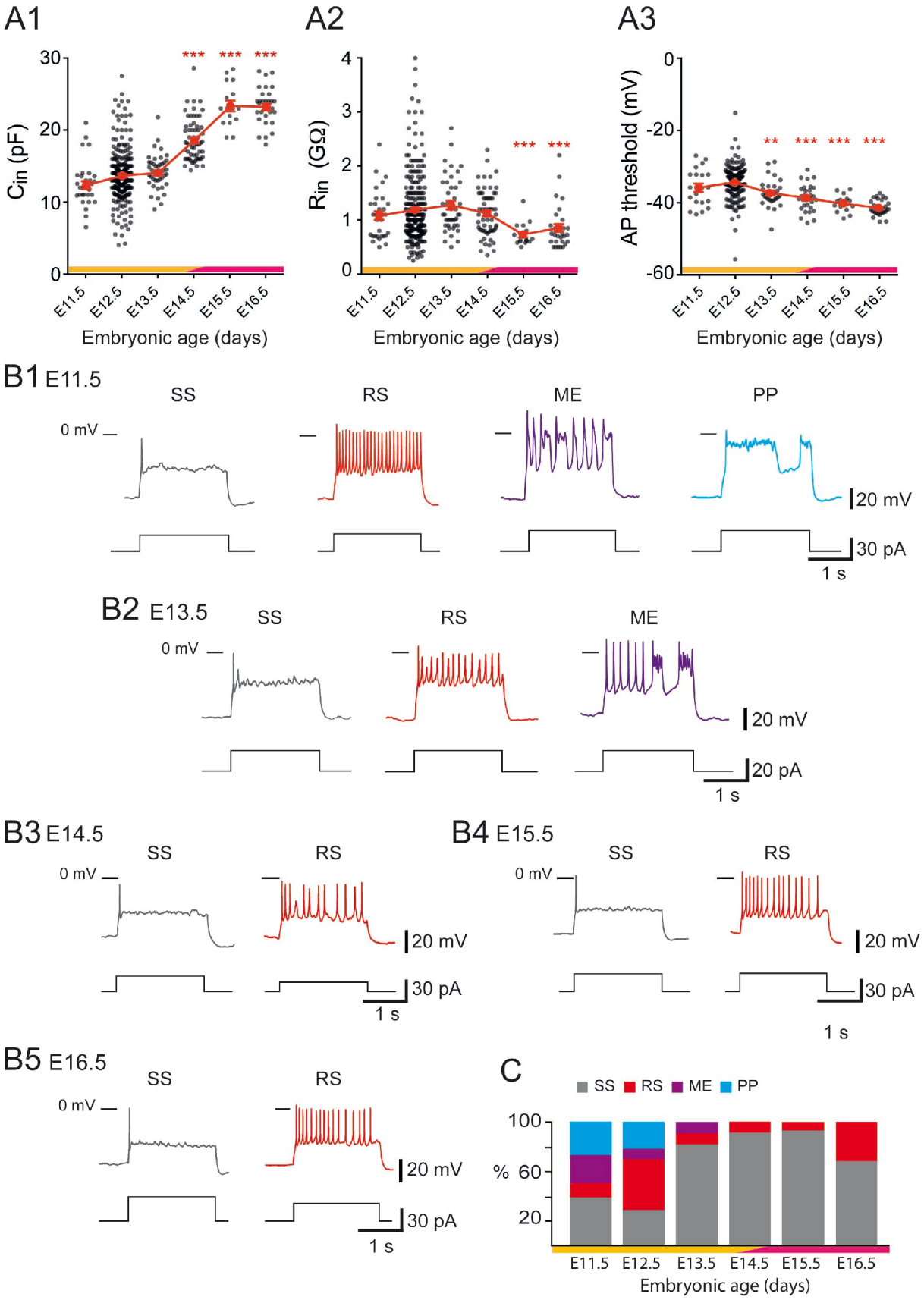
A1
A2
A3
Cin (pF)
Rin (GΩ)
AP threshold (mV)
Embryonic age (days)
E11.5
E12.5
E13.5
E14.5
E15.5
E16.5
B1 E11.5
B2 E13.5
B3 E14.5
B4 E15.5
B5 E16.5
SS
RS
ME
PP
0 mV
20 mV
30 pA
20 pA
1 s
C
%

Fig 4

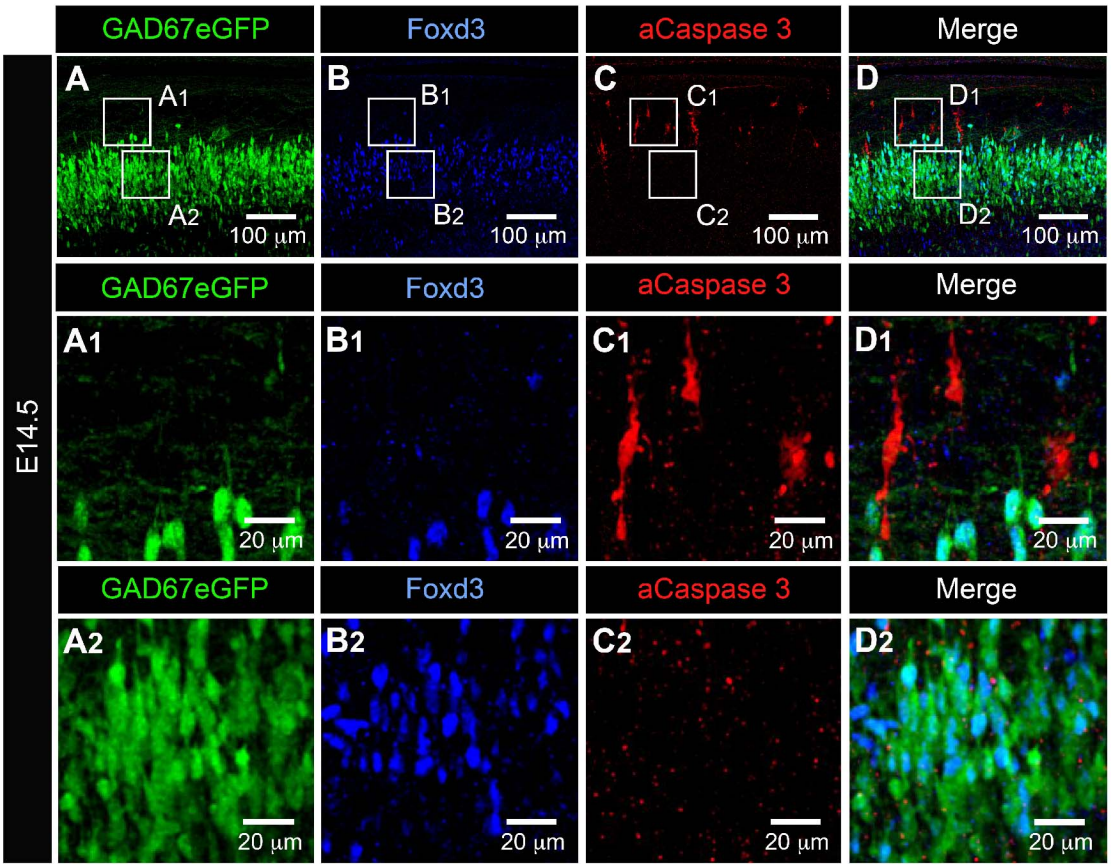
GAD67eGFP
Foxd3
aCaspase 3
Merge
E14.5
A
A1
A2
100 μm
B
B1
B2
100 μm
C
C1
C2
100 μm
D
D1
D2
100 μm
A1
B1
C1
D1
20 μm
A2
B2
C2
D2
20 μm

Fig 5

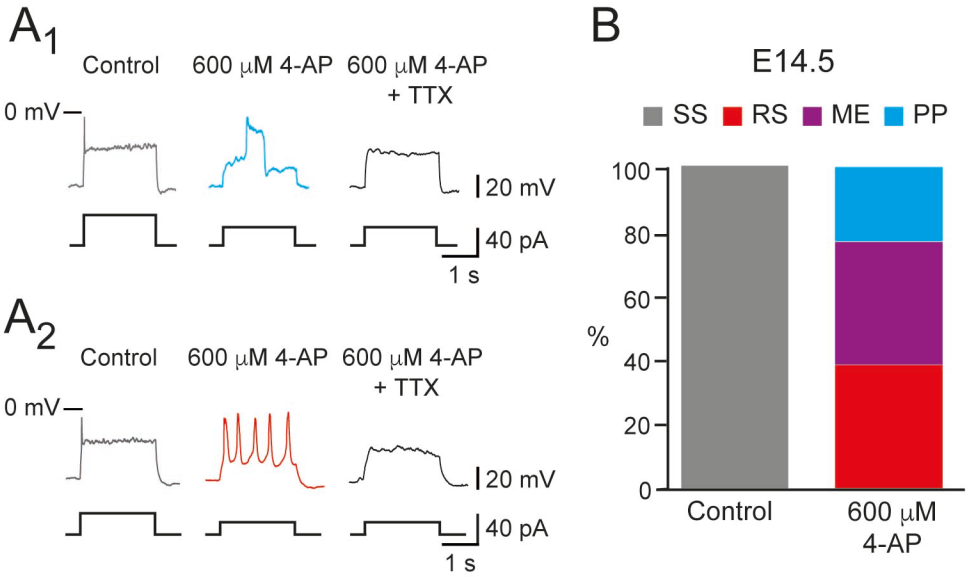
A1
Control
600 μM 4-AP
600 μM 4-AP
+ TTX
0 mV
20 mV
40 pA
1 s
A2
Control
600 μM 4-AP
600 μM 4-AP
+ TTX
0 mV
20 mV
40 pA
1 s
B
E14.5
SS
RS
ME
PP
100
80
60
40
20
0
%
Control
600 μM
4-AP

Fig 6

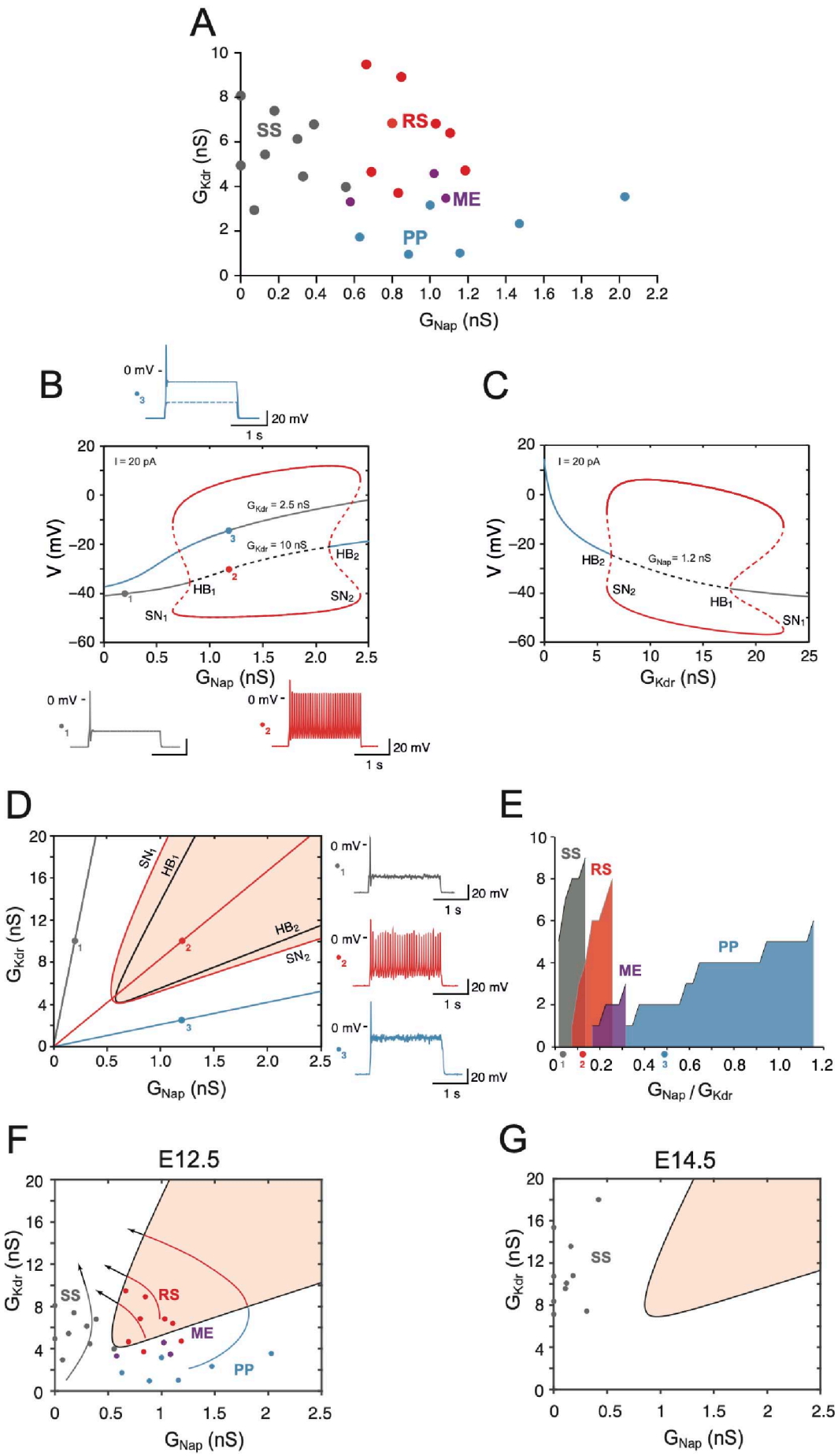
A
SS
RS
ME
PP
G_{Kdr} (nS)
G_{Nap} (nS)
B
0 mV
20 mV
1 s
I = 20 pA
G_{Kdr} = 2.5 nS
G_{Kdr} = 10 nS
HB1
HB2
SN1
SN2
V (mV)
G_{Nap} (nS)
C
I = 20 pA
G_{Nap} = 1.2 nS
HB2
SN2
HB1
SN1
V (mV)
G_{Kdr} (nS)
D
SN1
HB1
HB2
SN2
G_{Kdr} (nS)
G_{Nap} (nS)
E
SS
RS
ME
PP
G_{Nap} / G_{Kdr}
F
E12.5
SS
RS
ME
PP
G_{Kdr} (nS)
G_{Nap} (nS)
G
E14.5
SS
G_{Kdr} (nS)
G_{Nap} (nS)

Fig 7

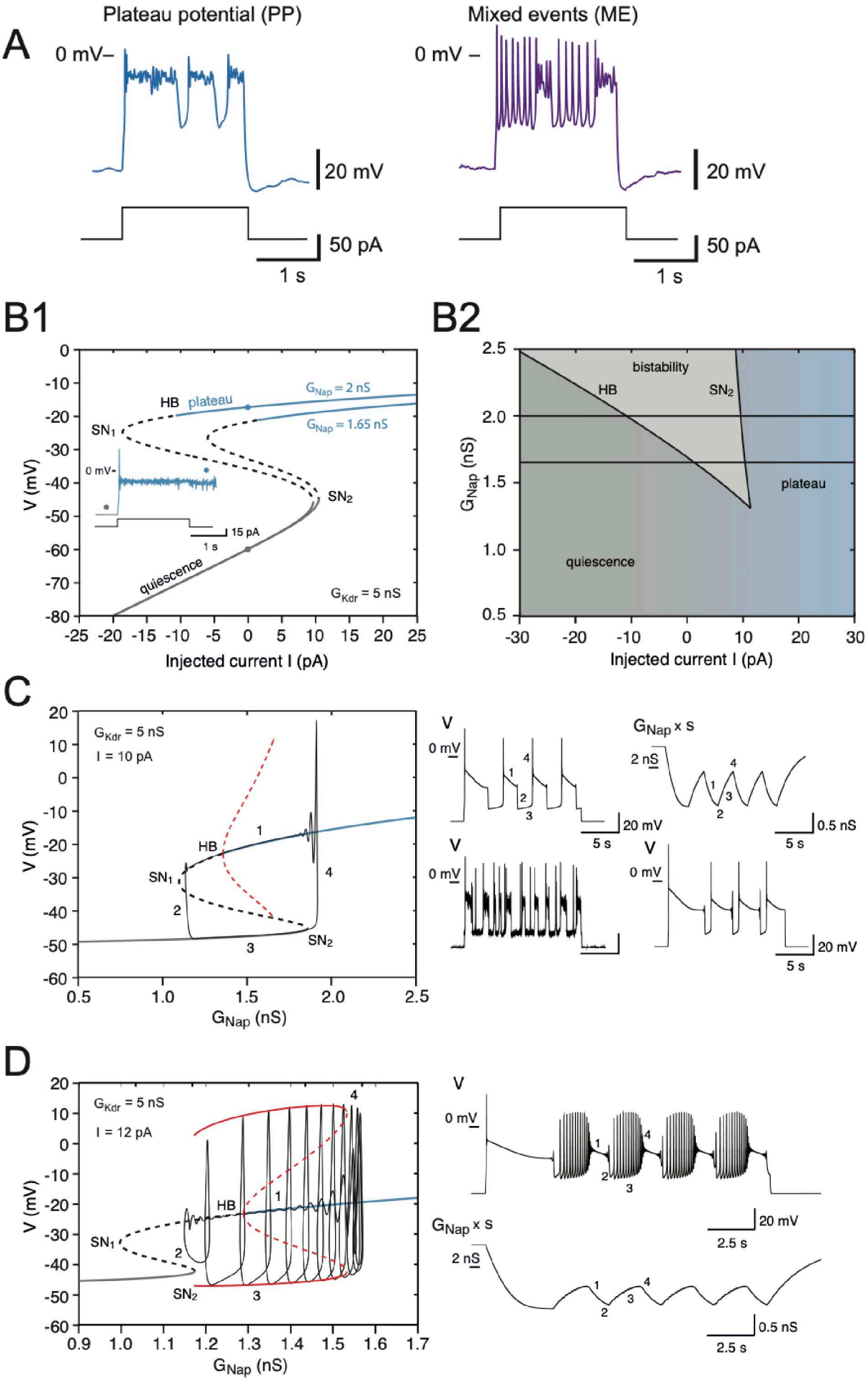
A
Plateau potential (PP)
Mixed events (ME)
0 mV
20 mV
50 pA
1 s
B1
B2
HB
plateau
SN1
SN2
quiescence
GNap = 2 nS
GNap = 1.65 nS
GKdr = 5 nS
15 pA
V (mV)
Injected current I (pA)
bistability
GNap (nS)
C
GKdr = 5 nS
I = 10 pA
GNap x s
2 nS
0.5 nS
5 s
D
I = 12 pA
2.5 s

Fig 8

Supplementary figures

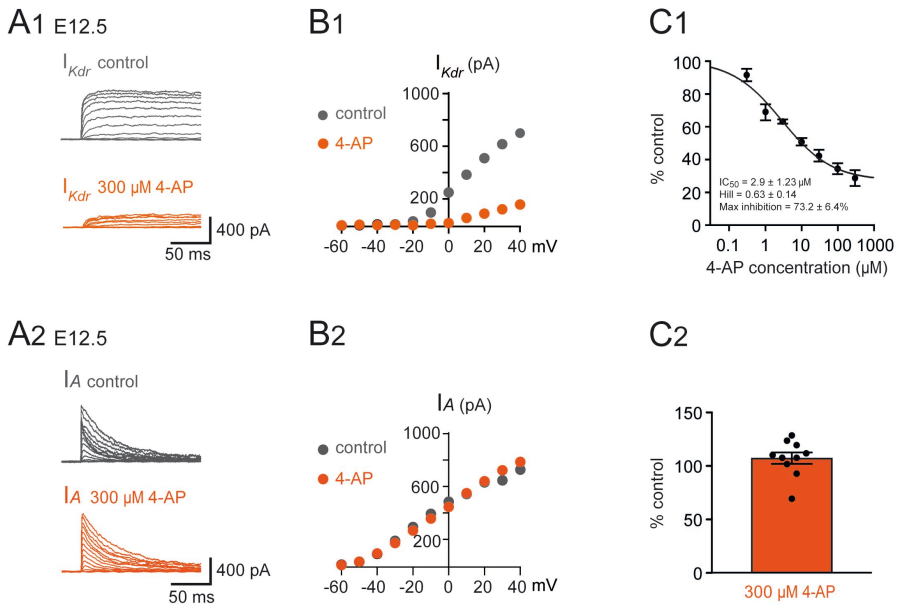

Figure 2—figure supplement 1. Effect of 4-AP on I_{Kdr} and I_A in embryonic V1^R
(A1) Example of voltage-dependent potassium currents evoked in response to 10 mV membrane potential steps (200 ms) from -100 mV or from -30 mV to +40 mV (10 s interval between pulses). V1^R were voltage clamped at V_H = -60 mV. A prepulse of -40 mV (300 ms) was applied to activate both I_A and I_{Kdr}. I_{Kdr} was evoked in response to 10 mV membrane potential steps (200 ms) from -100 mV to +40 mV. V1^R were voltage clamped at V_H = -60 mV. A prepulse of 30 mV (V_H = - 30 mV) was applied to isolate I_{Kdr}. (A1) Representative example of the effect of 300 µM 4-AP application on I_{Kdr} recorded from embryonic V1^R at E12.5. (B1) Curves showing current-voltage relationships of I_{Kdr} in control and in the presence of 300 µM 4-AP. Measurements were performed on traces shown in A1. (C1) Dose-response relationship of 4-AP-evoked I_{Kdr} inhibition (mean + SE). Data were normalized to I_{Kdr} amplitude measured in the absence of 4-AP (V_H = 40mV) and fitted as explained in Materials and Methods. Note that 4-AP IC_{50} is in µM range (2.9 µM). 0.3 µM 4-AP n = 3; N = 3, 1 µM 4-AP n = 3; N = 3, 3 µM 4-AP n = 9; N = 9, 10 µM 4-AP n = 13; N = 13, 30 µM 4-AP n = 7; N = 7, 100 µM 4-AP n = 7; N = 7, 300 µM 4-AP n = 7; N = 7. (A2) I_A was obtained as the difference between currents evoked from V_H = -100 mV and currents evoked from V_H = -30 mV (10 mV voltage step). (A2) Representative example of the effect of 300 µM 4-AP on I_A in V1^R recorded at E12.5. (B2) I_A Current-voltage ($I - V$) relationship in control conditions and in the presence of 300 µM 4-AP. The $I - V$ curves were obtained from the traces shown in A1. (C2) Bar graph showing the percentage of I_A block elicited by 4-AP. Note that 4-AP did not significantly block I_A (Wilcoxon test P = 0.065, n = 10).

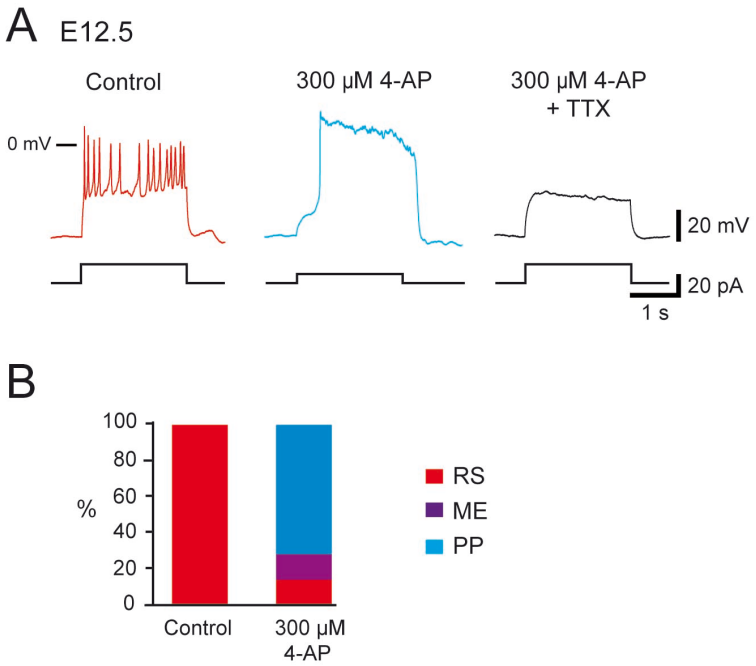

Figure 2—figure supplement 2. Relates to Fig 2. Effect of 4-AP application in repetitively spiking V1^R at E12.5

(A) Representative traces showing the effect of 4-AP application (300 µM) on Repetitive Spiking (RS) V1^R at E12.5. Note that plateau potential activity evoked in the presence of 4-AP (middle trace) was blocked by 0.5 µM TTX (right trace). (B) Bar plots showing the changes in the firing pattern of RS V1^R evoked by 300 µM 4-AP application (n = 14). 4-AP application evoked a plateau potential in 71.4 % of the recorded neurons (10/14) and mixed events in 14.3% of the recorded neurons (2/14). The excitability pattern was not modified in 2 neurons. Repetitive Spiking (RS) V1^R (red), Mixed events (ME) V1^R (purple), Plateau Potential (PP) V1^R (blue).

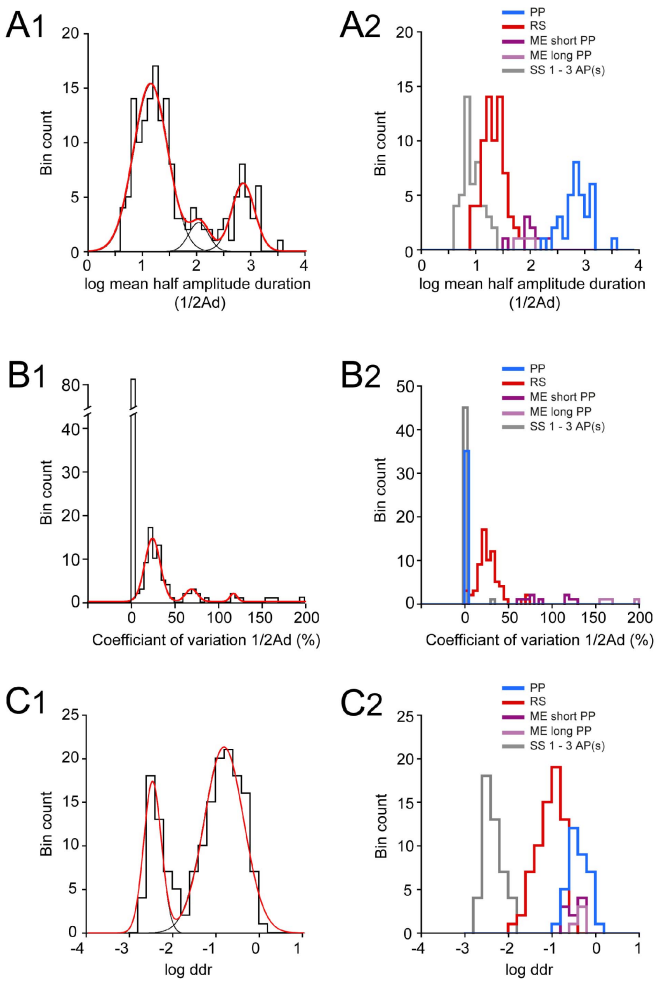

Figure 3—figure supplement 1. Distributions of log ½Ad, CV ½Ad and log ddr values related to the cluster analysis of embryonic V1^R firing patterns

(A1) Histogram of log mean ½Ad (mean half amplitude event duration) for the whole V1^R population at E12.5 (n= 164; bin width 0.1). The histogram was well fitted by the sum of three Gaussian curves with means and SDs of 1.135, 2.046 & 2.84, and 0.316, 0.181 & 0.21, respectively. (A2) Histogram of the values of log mean ½Ad sorted after cluster analysis showing single spiking (SS) V1^R (gray), repetitive spiking (RS) V1^R (red), mixed events (ME) V1^R with short plateau potentials (ME short PP V1^R, light purple), ME V1^R with long plateau potentials (ME long PP V1^R, dark purple) and plateau potential (PP) V1^R (blue). log mean ½Ad was significantly different between SS V1^R, PP V1^R, the whole ME V1^R population (ME$_S$ and ME$_I$ V1^R) and PP V1^R (Kruskall-Wallis test $P < 0.0001$; SS V1^R versus RS V1^R, $P < 0.0001$; SS V1^R versus ME V1^R, $P < 0.0001$; SS V1^R versus PP V1^R, $P < 0.0001$; RS V1^R versus ME V1^R, $P = 0.0004$; RS V1^R versus PP V1^R, $P < 0.0001$; ME V1^R versus PP V1^R, $P = 0.018$; SS V1^R n = 46, RS V1^R n = 69, ME$_S$ V1^R n = 9, ME$_I$ V1^R n = 4, PP V1^R n = 35). (B1) Histogram of CV ½Ad for the whole V1^R population at E12.5 (n= 164; bin width 5%). Note that a large population of V1^R had zero CV ½Ad (n = 83). The histogram for CV ½Ad ≠ 0 was fitted by the sum of three Gaussian curves with means and SDs of 23.4, 68.4 & 117 (%) and 8.9, 6.8 & 4.1, respectively. (B2) Histograms of the values of CV ½Ad sorted after cluster analysis showing SS V1^R (black), RS V1^R (red), ME$_S$ V1^R (light purple), ME$_I$ V1^R (dark purple) and PP V1^R. CV ½Ad was not significantly different between SS V1^R and PP V1^R (CV ½Ad of SS V1^R and PP V1^R = 0.682 % and 0% respectively: only one of the 46 SS V1^R displayed 3 PA and had a CV ½Ad of 31.37). CV ½Ad was significantly different between RS V1^R and the whole ME V1^R population and

also between SS $V1^R$ or PP $V1^R$ and RS $V1^R$ or ME $V1^R$ (Kruskall-Wallis test $P < 0.0001$; SS $V1^R$ versus RS $V1^R$ $P < 0.0001$, SS $V1^R$ versus ME $V1^R$ $P < 0.0001$, SS $V1^R$ versus PP $V1^R$ $P = 0.846$, RS $V1^R$ versus ME $V1^R$ $P = 0.0003$, RS $V1^R$ versus PP $V1^R$ $P < 0.0001$, ME $V1^R$ versus PP $V1^R$ $P < 0.0001$). (C1) Histogram of log ddr (sum of ½Ad divided by pulse duration) for the whole $V1^R$ population at E12.5 (n= 164; bin width 0.2). The histogram was fitted by the sum of two Gaussian curves with means and SDs of -2.51 & -0.851, and 0.2 & 0.46, respectively. (C2) Histograms of the values of log ddr sorted after cluster analysis showing SS $V1^R$ (black), RS $V1^R$ (red), ME_s $V1^R$ (light purple), ME_l $V1^R$ (dark purple) and PP $V1^R$. log (ddr) was not significantly different between ME $V1^R$ and PP $V1^R$, while it was significantly different between SS $V1^R$ and RS $V1^R$, SS $V1^R$ and the whole ME $V1^R$ population, SS $V1^R$ and PP $V1^R$, RS $V1^R$ and the whole ME $V1^R$ population, RS $V1^R$ and PP $V1^R$ (Kruskall-Wallis test $P < 0.0001$; SS $V1^R$ versus RS $V1^R$, $P < 0.0001$; SS $V1^R$ versus ME $V1^R$, $P < 0.0001$; SS $V1^R$ versus PP $V1^R$, $P < 0.0001$; RS $V1^R$ versus ME $V1^R$, $P < 0.0001$; RS $V1^R$ versus PP $V1^R$, $P < 0.0001$; ME $V1^R$ versus PP $V1^R$, $P = 0.977$). ME_s $V1^R$ and ME_l $V1^R$ differed only by their CV ½Ad (Mann-Whitney test, log mean ½Ad for ME_s $V1^R$ versus log mean ½Ad for ME_l $V1^R$, $P = 0.26$; CV ½Ad for ME_s $V1^R$ versus CV ½Ad ME_l $V1^R$, $P = 0.0028$ and log ddr for ME_s $V1^R$ versus log ddr for ME_l $V1^R$, $P = 0.1483$). It is noteworthy that the distribution of the values of each metric was multimodal thus indicating that each of them could partially discriminate different groups of embryonic $V1^R$ according to their firing pattern.

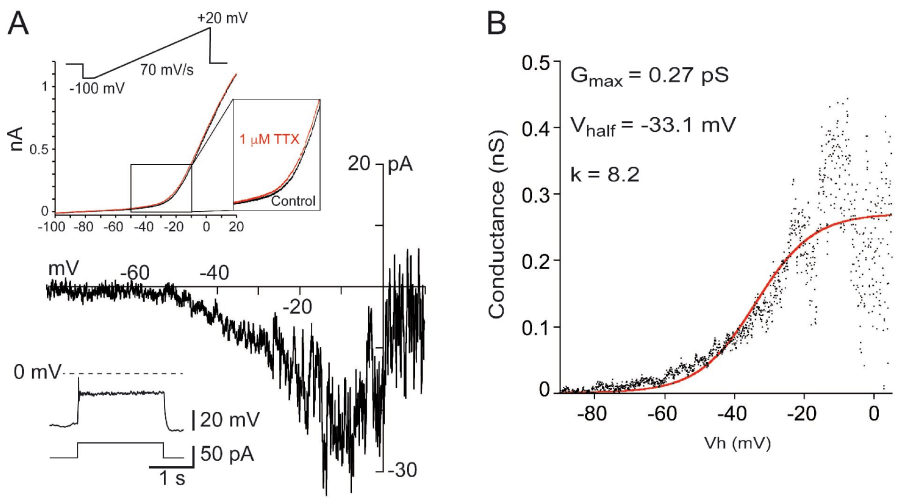

Figure 6—figure supplement 1. I_{Nap} is present in embryonic V1^R recorded at E14.5

(A) Representative trace of I_{Nap} evoked by a slow depolarizing voltage ramp (70 mV/s, upper insert) in SS embryonic V1^R (lower insert). I_{Nap} was isolated by subtracting currents evoked by depolarizing ramps in the presence of 1 μM TTX to the control current evoked in the absence of TTX (upper insert). (B) Voltage dependence of G_{Nap} conductance calculated from the trace shown in A. The activation curve was obtained by transforming the current evoked by a depolarizing voltage ramp from -100 mV to 20 mV (70 mV/s) using the following equation: $G_{NaP} = -I_{Nap}/((-Vh)+E_{Na})$ where Vh is the holding potential at time t during a depolarizing voltage ramp and E_{Na} is the equilibrium potential for sodium (E_{Na} = 60 mV). The G_{NaP}/Vh curve was fitted with the following Boltzmann function: $G = G_{MAX}/(1+\exp(-(V-V_{HALF})/k)))$ (Boeri et al. 2018), where V_{half} is the Vh value for G_{Nap} half activation, k the slope factor of the curve and G_{max} the maximum conductance. We found no significant difference between the values of V_{half} (Mann-Whitney test: P = 0.8518) and of k (Mann-Whitney test: P = 0.7546) obtained at E12.5 (Boeri et al. 2018) and those obtained at E14.5. At E14.5 V_{half} = -27 ± 5.1 mV and k = 7.73 ± 0.78 (n = 6).

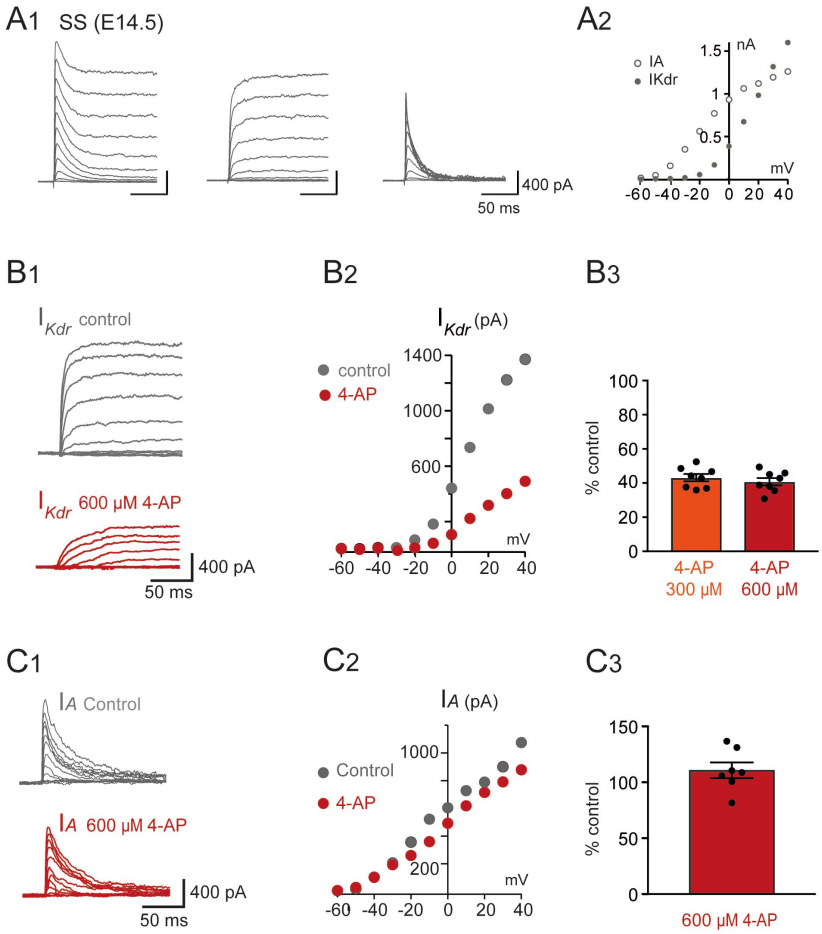

Figure 6—figure supplement 2. I_{Kdr} was inhibited by 4-AP in V1^R recorded at E14.5
(A1) Representative examples of the total outward K^+ currents obtained from V_H = -100 mV (left traces), of I_{Kdr} (V_H = -30 mV, middle traces) and of isolated I_A (left traces) recorded in single spiking (SS) V1^R at E14.5. (A2) Current-voltage relationship of I_{Kdr} (filled circle) and of I_A (open circle) in SS V1^R at E14.5. $I-V$ curves were obtained from currents shown in A1. (B1) Representative example of the effect of 4-AP at 600 µM in V1^R at E14.5. (B2) Current-voltage curves in control condition and in the presence of 600 µM 4-AP. (B3) Bar plots showing the percentage of I_{Kdr} inhibition evoked by 300 µM 4-AP application (n = 8) and by 600 µM 4-AP application (n = 7). The percentages of I_{Kdr} inhibition evoked by 300 µM 4-AP and by 600 µM 4-AP applications were not significantly different (P = 0.574). (C1) Representative example of the effect of 600 µM 4-AP on I_A in V1^R recorded at E14.5. (C2) $I-V$ curves in control conditions and in the presence of 600 µM 4-AP. These curves were obtained from the traces shown in B1. (C3) Bar graph showing the percentage of I_A block elicited by 4-AP. 4-AP did not significantly block I_A (Wilcoxon test P = 0.11, n = 6).

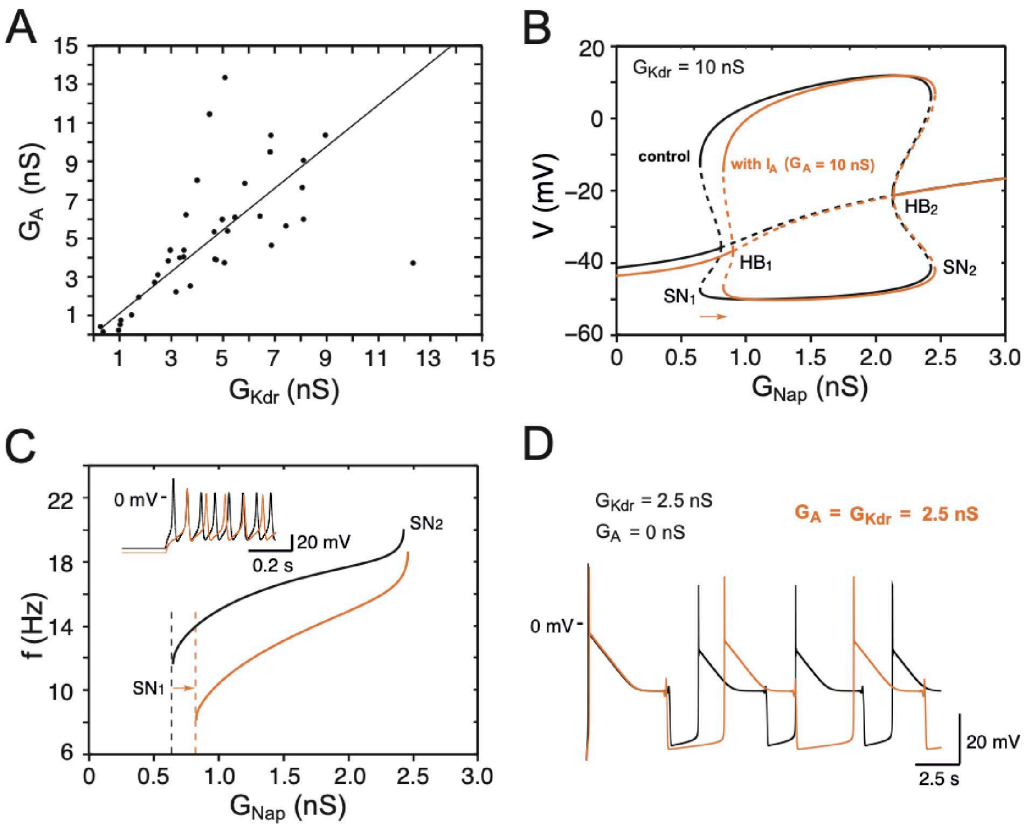

Figure 7—figure supplement 1. Effects of I_A on embryonic V1^R firing patterns predicted by computational modeling

(A) The maximal conductances of I_{Kdr} and I_A at E12.5 are linearly correlated. Best fit: G_A = 1.09 G_{Kdr} (R^2 = 0.81, N=44). (B) Effect of I_A on the dynamics of the basic model. The one-parameter bifurcation diagrams in control condition (black, I = 20 pA, G_{Kdr} = 10 nS, no I_A, same as in Fig 7B) and with I_A added (orange, G_A = 10 nS) are superimposed. The I_A current shifts the firing threshold SN_1 to the right by 0.18 nS (see also C) as indicated by the orange arrow, with little effect on the amplitude of action potentials (see also insert in C). In contrast, I_A shifts SN_2 by only 0.03 nS because it is inactivated by depolarization. (C) I_A also slows down the discharge frequency, as shown by comparing the $G_{Nap} - V$ curves without I_A (black) and with I_A (orange). For G_{Nap} = 1 nS, for instance, the firing frequency is reduced by 31%, from 15 to 10.4 Hz. Here again, the effect of I_A progressively decreases as G_{Nap} increases because of the membrane depolarization elicited by I_{Nap}. For G_{Nap} = 2.4 nS, for instance, the firing frequency is reduced by 11% only, from 19.1 to 17 Hz. This frequency reduction elicited by I_A does not merely result from the increased firing threshold. Note also that the latency of the first spike is increased (see voltage trace in insert), which is a classical effect of I_A. (D) I_A reduces the frequency of pseudo-plateau bursting by lengthening quiescent episodes (doubling their duration in the example shown) without affecting the duration of plateaus much (here a mere 5% increase), as shown by the comparison of the voltage traces obtained without I_A (control, $G_{Kdr} = 2.5$ nS, black) and with I_A ($G_{Kdr} = G_A = 2.5$ nS, orange). This is because I_A is activated near rest but inactivated during voltage plateaus. Note that increasing G_{Kdr}, in the absence of I_A has not the same effect; it shortens both plateaus and quiescent episodes (see Fig 8C, where $G_{Kdr} = 5$ nS). Again, this is because I_{Kdr} does not inactivate (or does it only very slowly), in contrast to I_A.

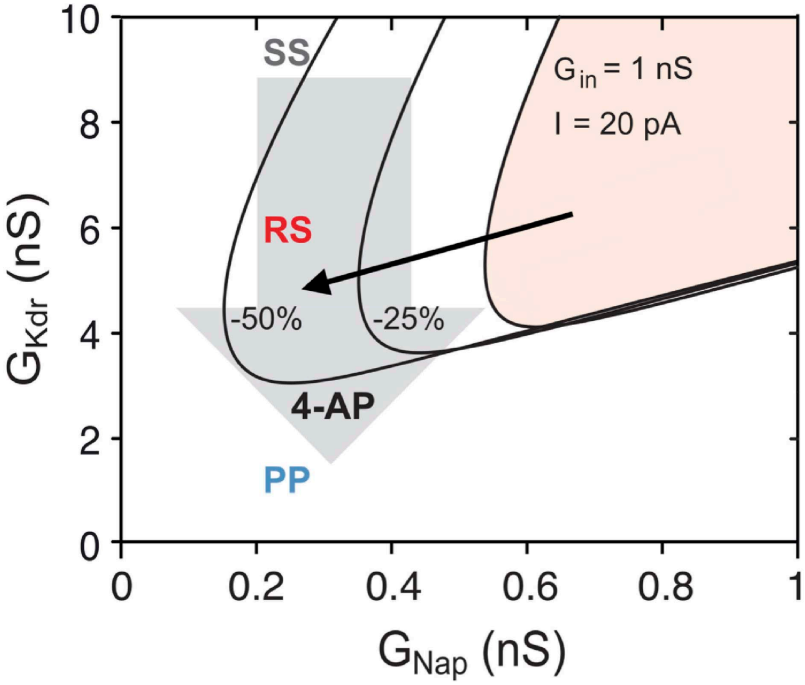

Figure 7—figure supplement 2. Explaining the effect of 4-AP on the firing pattern
The RS region of the basic model, where repetitive firing may occur, is displayed in the G_{Nap} – G_{Kdr} plane in control condition for E12.5 V1^{R} (C_{in} = 13 pF, G_{in} = 1 nS, I = 20 pA, shaded area), and when G_{in} and I were both reduced by 25% (middle curve) or by 50% (left curve). The reduced I accounts for the decrease in rheobase, and thus in the current injected in the experiments, following the decrease in G_{in}. If 4-AP reduced only G_{Kdr} (as indicated by the downward arrow) the firing pattern of SS V1^{R} would not change, the RS region being too far to the right to be visited. In contrast, when the effects of 4-AP on the input conductance and rheobase are taken into account, the bifurcation diagram moves leftwards and downwards, as indicated by the oblique black arrow, and the RS and PP regions are then successively entered as G_{Kdr} is reduced. The same explanation holds at E14.5.